Mathematical Modeling and Analysis of Spatial Neuron Dynamics: Dendritic Integration and Beyond

SONGTING LI
School of Mathematical Sciences, MOE-LSC
Institute of Natural Sciences
Shanghai Jiao Tong University

DAVID W. MCLAUGHLIN
Courant Institute
Center for Neural Science
Neuroscience Institute of NYU Langone Health
New York University
NYU-ECNU Institute of Mathematical Sciences
New York University Shanghai

AND

DOUGLAS ZHOU
School of Mathematical Sciences, MOE-LSC
Institute of Natural Sciences
Shanghai Jiao Tong University

Abstract

Neurons compute by integrating spatiotemporal excitatory (E) and inhibitory (I) synaptic inputs received from the dendrites. The investigation of dendritic integration is crucial for understanding neuronal information processing. Yet quantitative rules of dendritic integration and their mathematical modeling remain to be fully elucidated. Here neuronal dendritic integration is investigated by using theoretical and computational approaches. Based on the passive cable theory, a PDE-based cable neuron model with spatially branched dendritic structure is introduced to describe the neuronal subthreshold membrane potential dynamics, and the analytical solutions in response to conductance-based synaptic inputs are derived. Using the analytical solutions, a bilinear dendritic integration rule is identified, and it characterizes the change of somatic membrane potential when receiving multiple spatiotemporal synaptic inputs from the dendrites. In addition, the PDE-based cable neuron model is reduced to an ODE-based point-neuron model with the feature of bilinear dendritic integration inherited, thus providing an efficient computational framework of neuronal simulation incorporating certain important dendritic functions. The above results are further extended to active dendrites by numerical verification in realistic neuron simulations. Our work provides a comprehensive and systematic theoretical and computational framework for the study of spatial neuron dynamics. © 2021 The Authors. *Communications on Pure and Applied Mathematics* published by Wiley Periodicals LLC.

Communications on Pure and Applied Mathematics, 0001–0049 (PREPRINT)

Contents

1 Introduction

Dendrites play an essential role in neuronal computation. In the brain, a neuron in general receives many excitatory (E) and inhibitory (I) synaptic inputs along its dendrites, and changes its membrane potential at the soma by integrating these synaptic inputs. This process is known as dendritic integration [42, 45]. Experiments have demonstrated that the dendritic integration of synaptic inputs is crucial for supporting complex brain functions. For instance, dendritic integration is able to enhance motion detection [20, 21], to shape spiking activity [13, 69], and to promote information coding [6, 12]. In addition, dendritic integration fine tunes brain rhythms by modulating the frequency [2] and improving the robustness [84] of neuronal oscillations.

Dendritic integration is influenced by multiple factors in complicated ways. Before the generation of neuronal output signals known as action potentials, an individual excitatory postsynaptic potential (EPSP) or inhibitory postsynaptic potential (IPSP) needs to spread from the dendritic site of their origin to the action potential initiation zone. The propagation of a postsynaptic potential is substantially affected by both the passive and active properties of dendrites that determine the propagation speed and the modulation of the postsynaptic potential amplitude [31, 75]. When two or more synaptic inputs are received, the integration of them is in general influenced by their spatial and temporal properties [4, 24, 42, 76, 80]. Recent *in vitro* and *in vivo* experiments further show that the integration of synaptic potentials can be linear [10, 11], sublinear [43, 87], or supralinear [23, 85] under different experimental conditions. Despite a variety of observations for dendritic integration, a quantitative characterization of the integration rules for synaptic inputs along with their mechanistic understanding remain to be fully clarified.

In addition to many experiments, the rules of dendritic integration have also been under active investigations from theoretical and computational perspectives [32, 35, 40, 41, 53]. The computational approach subdivides a neuron into multiple interconnected compartments, and simulates the current flow in each compartment modeled as a resistance-capacitance circuit obeying Kirchhoff's law [57]. The simulation of a multicompartment neuron model enables one to study numerically

the response of a neuron when receiving multiple synaptic inputs from its dendrites, and has been used to investigate many aspects of dendritic integration. For instance, based on the multicompartment neuron simulation, it is discovered that the nonlinear integration of synaptic inputs mainly takes place within dendritic branches locally [36], yielding the computation of logical operations. In addition, the synaptic inputs are found to be first integrated nonlinearly within each branch, followed by a linear integration of the branch outputs at the soma [32,53,54]. These simulation phenomena are supported by experiments [6,33]. A recent work further shows that the integration of *in vivo*–like synaptic inputs can be well captured by linear integration with a single global dendritic nonlinearity [83]. Despite the fact that the computational approach can help gain insights into rich phenomena of spatiotemporal dynamics observed at the dendrites, a deep and comprehensive understanding of dendritic integration requires analytical approaches, as also pointed out in references [42,70].

As an effective analytical framework, the cable theory based on partial differential equations (PDEs) was developed to describe mathematically the dynamical response of a passive neuron with dendritic structures when a neuron receives synaptic inputs [57,71]. The theory focuses on the subthreshold regime of neuronal membrane potential, in which voltage-gated channels are weakly activated; hence the dendrites can be considered as a passive cable. The cable theory has been successfully applied to characterize and estimate the electrical properties of dendrites and synapses in the absence of action potentials [25, 49, 58, 59, 62–64, 68]. The analytical solution of an unbranched dendritic cable of finite length in response to nonuniform current inputs was obtained to describe the shape of EPSP [56]. The solution for current input to a single branch of a special dendritic tree was later provided by using the principle of superposition [61, 66]. Furthermore, the analytical solution for dendritic trees with arbitrary branching structures was also calculated [48]. The solvability of the cable neuron model under injected current inputs attributes to the linearity of the equation, which allows one to apply the Green's function method. However, neurons communicate via synaptic currents. Consequently, the membrane potential depends nonlinearly on the synaptic conductance input [34], which greatly complicates mathematical analysis. In order to solve the cable model under conductance-based synaptic inputs analytically, one usually makes the approximation of constant synaptic conductance [28, 81], or analyzes the steady state of neuronal response by assuming that both the synaptic conductance and the membrane potential are constant [24, 34, 38, 39, 88]. Such analyses usually oversimplify the spatial aspect of dendritic integration, and fail to describe the temporal aspect of dendritic integration, as discussed in detail below.

Based on perturbation analysis, analytical solutions of an unbranched passive cable neuron model with conductance-based spatiotemporal synaptic inputs have been derived by the authors recently [40, 41]. The analytical solutions reveal the mechanism underlying a bilinear rule of dendritic integration that quantifies the

spatial summation of a pair of E and I inputs [24], and further generalize the bilinear rule to characterize the spatiotemporal summation of a pair of E and I inputs, a pair of E inputs, a pair of I inputs, and multiple E and I inputs [40]. The generalized rule states that, when a neuron receives two or more synaptic inputs, the neuronal response at the soma can be well approximated by the linear summation of all individual postsynaptic potentials induced by each input received alone, with additional bilinear interactions between all the paired synaptic inputs. By accounting for the active property of dendrites, the rule is verified via realistic neuronal simulations and electrophysiological experiments [24, 40, 41]. The above analysis is limited to the cable neuron model of an unbranched dendrite, in which a neuron receives synaptic inputs only from the dendritic trunk. In this work, a comprehensive analysis of the cable neuron model with spatially branched dendritic structure is presented, and dendritic integration is analytically investigated for arbitrary branched dendrites, thus establishing that the bilinear dendritic integration rule is valid in the realistic *in vivo* case of branched dendrites. Provided with a valid mathematical foundation, this general bilinear dendritic integration rule offers important insights into the understanding of dendritic computation.

Although being capable of capturing many aspects of dendritic multi-integration and computations, cable neuron models and the related multicompartment neuron models are computationally expensive. To be specific, one is required to numerically solve hundreds of differential equations for each neuron in a simulation. This presents a challenge for the simulation of large-scale neuronal networks composed of millions of neurons, e.g., the number of neurons in the primary visual cortex of primates, not to mention the whole brain network. In contrast, point neuron models are computationally feasible for large-scale cortical network simulations. Many point neuron models have been developed to describe the dynamics of the membrane potential at the soma of a neuron [19, 26, 30, 37, 51, 67, 72]. Despite their broad applications, these point neuron models fail to capture dendritic computations. Efforts have been made to incorporate dendritic features into point neuron models phenomenologically [32, 53, 54, 83]. However, the form of these models varies under different synaptic input conditions. In addition, the determination of the parameters in these models requires case-by-case experimental data fitting. Both facts weaken the biological insights and practical applications of these phenomenological models. Previously a point-neuron model with dendritic integration incorporated had been derived by the authors based on the analysis of an idealized static electrical circuit model [39]. The model is named as the dendritic integrate-and-fire (DIF) model. The structure of the DIF model has a clear biological interpretation and has been verified in realistic neuron simulations and electrophysiological experiments [39]. However, the derivation of the DIF model was restricted to the simple case of static input to the electrical circuit model. Here, based on the analysis of the spatially branched cable neuron model with realistic

time varying synaptic inputs, the original PDE-based model is mathematically reduced to the ODE-based DIF model with the appropriately inherited properties of dendritic integration.

In this work, the aforementioned questions related to dendritic integration will be addressed using both theoretical and computational approaches. Nonlinear dendritic integration can arise in both passive and active dendrites. Here passive but realistically branched dendrites are treated analytically, and the results are generalized computationally to the case of active branched dendrites. In Section 2, a PDE-based cable neuron model is used to represent the subthreshold membrane potential dynamics of a neuron with spatially branched dendritic structure, followed with a realistic cable neuron model that adds active ion channels to the passive cable model. In Section 3, analytical solutions to the PDE-based passive cable neuron model in response to time-varying synaptic inputs are derived. Based on these analytical solutions, a bilinear dendritic integration rule is identified, which characterizes the somatic membrane potential's response when a neuron receives multiple spatiotemporal synaptic inputs distributed along the branched dendrites. In Section 4, the PDE-based cable neuron model is reduced to an ODE-based point-neuron model with the feature of bilinear dendritic integration inherited. Then an efficient computational framework is proposed for neuronal simulations that incorporate important dendritic functions. Note that "regular perturbation analysis" is sufficient to justify and validate the reduced point-neuron model. All of the above conclusions are extended to active dendrites with stronger synaptic inputs through numerical simulations of neurons with realistic branched dendrites. In Section 5, our main results are summarized, as are the limitations of the current study and possible directions of the future work.

Our goal in this work is to describe, in rather complete mathematical detail, an analytical study of a realistic branched passive cable model, with time-dependent synaptic inputs of moderate strength. This analytical study provides a detailed understanding of the mechanisms underlying dendritic integration. We also show, via numerical simulations, that these mechanisms extend to cases beyond the validity of the perturbation analysis, namely, to realistic models of active branched dendrites with stronger time-dependent synaptic inputs.

The novelty of this study is twofold. First, it develops an analytical approach to understand the properties of dendritic integration in a spatial neuron with branched dendrites—for instance, how dendritic computation quantitatively depends on the spatiotemporal properties of synaptic inputs. Second, it derives an effective point-neuron model asymptotically reduced from the cable model with branched dendrites, which further leads to a fast algorithm for the simulation of large-scale neuronal networks with dendritic integration incorporated. In contrast, the existing point neuron models, albeit computationally efficient, fail to capture the dendritic integration effect. Partial versions of some of these results (with little mathematical detail) have been published previously [38–40]; however, these partial results were

restricted to cable models of unbranched dendrites, with static synaptic inputs, or to both restrictions.

2 Neuron Models

In this section, the mathematical model of a passive cable neuron is first introduced, followed by the realistic neuron model that adds active ion channel dynamics to the cable neuron model. All the theoretical derivations and analyses in this work are based on the passive cable neuron model, and the validations and generalizations of the theoretical results are carried out by simulating the realistic neuron model numerically.

2.1 Cable neuron model

The passive neuron model is composed of a soma and branched dendrites. As shown in Figure 2.1, the model neuron possesses a realistic morphological structure reconstructed from experimental measurement [7]. The neuronal morphology is subdivided into interconnected cylindrical segments for later analysis and simulation. Dendritic segments are labeled with numbers and the local spatial coordinate is used at each segment. As an illustration, the neuronal membrane potential relative to the resting potential at location x and at time t on the i^{th} segment is denoted by $v_i(x,t)$, where $x \in [0, l_i]$ is the local coordinate on the i^{th} segment, and l_i is the length of the i^{th} segment. By convention, $x = 0$ refers to the end of the segment closer to the soma, and $x = l_i$ refers to the other end of the segment further away from the soma. For the ease of mathematical description, the global spatial coordinate is also used and is defined as $\boldsymbol{x} = (i, x)$. Accordingly, $v_i(x,t) = v(\boldsymbol{x},t)$. It is worth emphasizing that the bold symbol $\boldsymbol{x}$ is used to describe the global coordinate, distinguishing it from the local coordinate x.

The derivation of the model is based on the cable theory developed by Wilfrid Rall [57, 71]. Experiments show that the membrane of a neuron can be viewed as an electrical circuit composed of capacitors and resistors [14, 82]. When one focuses on a small segment $[x, x+\Delta x]$ on the i^{th} dendritic segment with diameter d_i, as illustrated in Figure 2.1, various types of electrical currents can be measured, including the capacitance current, the leak ionic current, the synaptic current, and the axial current. The capacitance current takes the form of

$$I_{\text{cap}} = c_i \frac{\partial v_i}{\partial t} \pi d_i \Delta x + o(\Delta x),$$

where c_i is the capacitance per unit area of membrane, and $o(\Delta x)$ includes all higher-order terms. And the leak channel current obeys Ohm's law, i.e.,

$$I_{\text{leak}} = -g_{Li} v_i \pi d_i \Delta x + o(\Delta x),$$

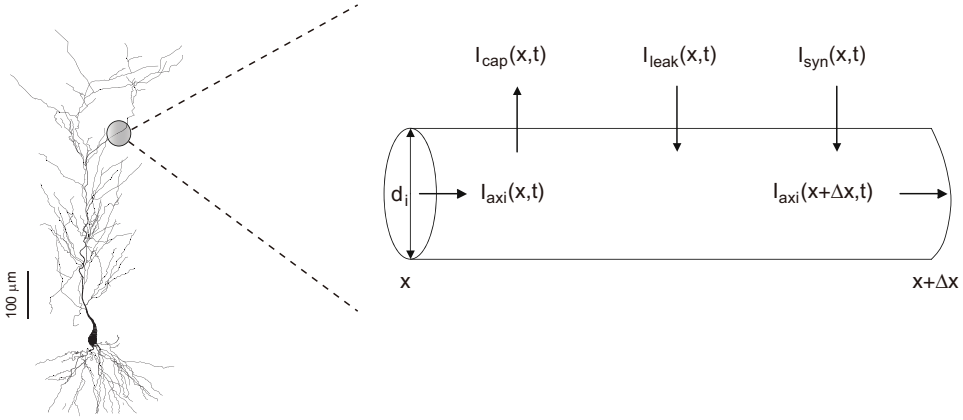

FIGURE 2.1. The cable neuron model. Left is the morphology of the model neuron. Right demonstrates four types of currents within a dendritic segment.

where g_{Li} is the leak conductance per unit area of membrane. In addition, the synaptic current also obeys Ohm's law,

$$I_{\text{syn}} = -\sum_{q=E,I} g_q(v_i - \varepsilon_q)\pi d_i \Delta x + o(\Delta x), \tag{2.1}$$

where g_E and g_I are the E and I synaptic conductance densities, and ε_E and ε_I are their reversal potentials relative to the resting potential, respectively. When the neuron receives multiple E and I inputs, g_q is the linear summation of all individual conductance transients with type q, i.e.,

$$g_q = \sum_j g_{q_j}$$

for $q = E, I$. For the j^{th} synaptic input of type q received at time $t = t_{q_j}$ and at site $\boldsymbol{x} = \boldsymbol{x}_{q_j}$, one has

$$g_{q_j} = f_{q_j} u_{q_j} \delta(\boldsymbol{x} - \boldsymbol{x}_{q_j}), \tag{2.2}$$

where f_{q_j} is the input strength of synaptic conductance, u_{q_j} is the normalized conductance, and $\delta(\cdot)$ is the Dirac delta function. The normalized conductance u_{q_j} is often modeled as [16–18]

$$\frac{du_{q_j}}{dt} = \alpha \cdot [T] \cdot (1 - u_{q_j}) - \beta \cdot u_{q_j}, \tag{2.3}$$

where u_{q_j} is interpreted as the fraction of open synaptic receptors, α and β are forward and backward rate constants for neurotransmitter binding, and $[T]$ is the transmitter concentration. u_{q_j} starts to evolve as equation (2.3) at time t_{q_j} when the neurotransmitter is released; thus it is denoted by $u_{q_j}(t; t_{q_j})$ below. Finally,

the axial current $I_{\text{axi}}(x)$ at location x on the i^{th} dendritic segment is proportional to the gradient of membrane potential, which can be derived from Ohm's law as

$$I_{\text{axi}}(x) = -\frac{\pi d_i^2}{4r_i}\frac{\partial v_i}{\partial x}\bigg|_x, \tag{2.4}$$

where r_i is the axial resistivity of the i^{th} segment.

Applying the law of current conservation to the small segment $[x, x+\Delta x]$ on the i^{th} segment leads to $I_{\text{cap}} = I_{\text{leak}} + I_{\text{syn}} + I_{\text{axi}}(x) - I_{\text{axi}}(x+\Delta x)$, i.e.,

$$\begin{aligned} c_i\frac{\partial v_i}{\partial t}\pi d_i\Delta x = &-g_{Li}v_i\pi d_i\Delta x - \sum_{q=E,I} g_q\cdot(v_i-\varepsilon_q)\pi d_i\Delta x \\ &- \frac{\pi d_i^2}{4r_i}\frac{\partial v_i}{\partial x}\bigg|_x + \frac{\pi d_i^2}{4r_i}\frac{\partial v_i}{\partial x}\bigg|_{x+\Delta x} + o(\Delta x). \end{aligned} \tag{2.5}$$

Dividing both sides of equation (2.5) by Δx, and taking the limit $\Delta x \to 0$, equation (2.5) becomes the cable equation describing the dynamics of the membrane potential on the i^{th} dendritic segment in response to spatiotemporal synaptic inputs,

$$c_i\frac{\partial v_i}{\partial t} = -g_{Li}v_i - g_E(v_i-\varepsilon_E) - g_I(v_i-\varepsilon_I) + \frac{d_i}{4r_i}\frac{\partial^2 v_i}{\partial x^2}, \tag{2.6}$$

with the conductance

$$g_q(\boldsymbol{x}, t; \{\boldsymbol{x}_{q_j}, t_{q_j}\}) = \sum_{j=1}^{n_q} f_{q_j} u_{q_j}(t; t_{q_j})\delta(\boldsymbol{x}-\boldsymbol{x}_{q_j}),$$

and n_q is the total number of the synaptic inputs of type $q = E, I$. It is worth mentioning the fact that the neuron response v_i depends nonlinearly on the synaptic input strength f_{q_j}, which will be discussed in detail below.

The boundary conditions of the cable neuron model (equation (2.6)) are proposed as follows. The dendritic branch connecting to the soma is first considered. Applying the law of current conservation at the soma leads to

$$c_s S\frac{\partial v_s}{\partial t} = -g_{Ls}Sv_s + I_{\text{dend}},$$

where S is the somatic membrane area, v_s is the somatic membrane potential, c_s is the capacitance per unit area of membrane at the soma, and g_{Ls} is the leak conductance per unit area of membrane at the soma. The dendritic current flowing to the soma, I_{dend}, takes the form of equation (2.4) at $x = 0$ on the dendritic segment connecting to the soma, which is labeled by index $i = 1$ in the following. Because the membrane potential is continuous at the connection point between the first dendritic segment and the soma, i.e., $v_s(t) = v_1(0,t)$, the boundary condition on this dendritic branch at $x = 0$ becomes

$$c_s\frac{\partial v_1}{\partial t}\bigg|_{x=0} = -g_{Ls}v_1(0,t) + \frac{\pi d_1^2}{4Sr_1}\frac{\partial v_1}{\partial x}\bigg|_{x=0}. \tag{2.7}$$

For the dendritic segments on the tip of the dendrites labeled by $\{i_m\}$, because the ends of these segments are sealed, the boundary conditions on these segments at $x = l_{i_m}$ are obtained as

$$\left.\frac{\partial v_{i_m}}{\partial x}\right|_{x=l_{i_m}} = 0. \tag{2.8}$$

Additional boundary conditions are prescribed at the connection site of several segments. Suppose that one end of several downstream segments labeled by $\{i_n\}$ with diameter $d_{i_1}, d_{i_2}, \ldots, d_{i_k}$ and length $l_{i_1}, l_{i_2}, \ldots, l_{i_k}$, respectively, are connected to the end of the upstream segment i with diameter d_i and length l_i. Applying the law of current conservation at the connection point leads to the following boundary conditions:

$$\left.\frac{\pi d_i^2}{4r_i}\frac{\partial v_i}{\partial x}\right|_{x=l_i} - \sum_{n=1}^{k}\left.\frac{\pi d_{i_n}^2}{4r_{i_n}}\frac{\partial v_{i_n}}{\partial x}\right|_{x=0} = 0. \tag{2.9}$$

In addition, the continuity of membrane potential at the connection point gives

$$v_i(l_i, t) = v_{i_1}(0, t) = v_{i_2}(0, t) = \cdots = v_{i_k}(0, t). \tag{2.10}$$

The initial condition of the neuron is simply set as $v_i(x, 0) = 0$, which corresponds to the resting state of the neuronal membrane potential before the neuron receives any input.

In the special case of an unbranched cylindrical dendrite connecting to an isotropic soma with homogeneous cable properties, the cable neuron model (equations (2.6)-(2.10)) reduces to the following ball-and-stick model,

$$c\frac{\partial v}{\partial t} = -g_L v - g_E(v - \varepsilon_E) - g_I(v - \varepsilon_I) + \frac{d}{4r}\frac{\partial^2 v}{\partial x^2}, \tag{2.11}$$

with boundary conditions

$$c\left.\frac{\partial v}{\partial t}\right|_{x=0} = -g_L v(0, t) + \left.\frac{\pi d^2}{4Sr}\frac{\partial v}{\partial x}\right|_{x=0}, \tag{2.12}$$

$$\left.\frac{\partial v}{\partial x}\right|_{x=l} = 0. \tag{2.13}$$

2.2 Detailed biophysical neuron model

The realistic neuron model is a biologically realistic modification of the passive cable neuron model (equations (2.6)-(2.10)) introduced above. Active ion channel currents are added to each dendritic segment, including voltage-gated sodium conductance g_{Na}, the delayed rectifier potassium conductance g_{K_d}, two variants of A-type potassium conductance $g_{K_A}^p$ and $g_{K_A}^d$ that are applied to the proximal and distal dendrites respectively, and the hyperpolarization-activated conductance g_h. The ionic current is described as $I_{\text{ion}} = g_{\text{ion}}(E_{\text{rev}} - V)$, where V is the postsynaptic potential, E_{rev} is the reversal potential, and g_{ion} is the ionic channel conductance.

The temporal dynamics of these ion channel currents will be introduced in this subsection, and their spatial distribution along the dendrites will be introduced in the next subsection.

The sodium conductance on the dendrites takes the form of $g_{Na} = f_{Na} m^3 h s$, where

$$\begin{aligned}
\frac{d\theta}{dt} &= \frac{\theta_\infty - \theta}{\tau_\theta}, && \theta = m, h, s,\\
\tau_m &= \frac{1}{[\alpha_m(V) + \beta_m(V)]Q_T}, && m_\infty = \frac{\alpha_m(V)}{\alpha_m(V) + \beta_m(V)},\\
\tau_h &= \frac{1}{[\alpha_h(V) + \beta_h(V)]Q_T}, && h_\infty = \frac{1}{1 + e^{(V+50)/4}},\\
\tau_s &= \frac{\beta_s(V)}{3 \times 10^{-4}[1 + \alpha_s(V)]}, && s_\infty = 1,
\end{aligned}$$

with

$$\begin{aligned}
\alpha_m(V) &= \frac{0.4(V + 30)}{1 - e^{-(V+30)/7.2}}, & \beta_m(V) &= \frac{-0.124(V + 30)}{1 - e^{(V+30)/7.2}},\\
\alpha_h(V) &= \frac{0.03(V + 45)}{1 - e^{-(V+45)/1.5}}, & \beta_h(V) &= \frac{-0.01(V + 45)}{1 - e^{(V+45)/1.5}},\\
\alpha_s(V) &= \frac{e^{139.23(V+60)}}{273.16 + T}, & \beta_s(V) &= \frac{e^{27.85(V+60)}}{273.16 + T},
\end{aligned}$$

and $T = 34^\circ$C is the temperature in unit of Celsius, $Q_T = 2$ is the temperature adjustment factor.

The delayed rectifier potassium conductance takes the form of $g_{K_d} = f_{K_d} n$, where

$$\frac{dn}{dt} = \frac{n_\infty - n}{\tau_n}, \quad \tau_n = \frac{\beta_n(V)}{0.02[1 + \alpha_n(V)]Q_T}, \quad n_\infty = \frac{1}{1 + \alpha_n(V)},$$

with

$$\alpha_n(V) = e^{\frac{-34.81(V-13)}{273.16+T}}, \quad \beta_n(V) = e^{\frac{-24.37(V-13)}{273.16+T}},$$

and with $T = 34^\circ$C and $Q_T = 1$.

For the A-type potassium conductance at the proximal dendrites less than 100 μm away from the soma, one has $g^p_{K_A} = f^p_{K_A} k l$, where

$$\begin{aligned}
\frac{d\theta}{dt} &= \frac{\theta_\infty - \theta}{\tau_\theta}, && \theta = k, l,\\
\tau_k &= \frac{\beta_k(V)}{0.1[1 + \alpha_k(V)]Q_T}, && k_\infty = \frac{1}{1 + \alpha_k(V)},\\
\tau_l &= 0.26(V + 50), && l_\infty = \frac{1}{1 + \alpha_l(V)},
\end{aligned}$$

with

$$\alpha_k = e^{\frac{11.60\zeta(V-11)}{273.16+T}}, \quad \beta_k = e^{\frac{6.38\zeta(V-11)}{273.16+T}},$$
$$\alpha_l = e^{\frac{35(V+56)}{273.16+T}}, \qquad \zeta = -1.5 - \frac{1}{1+e^{(V+40)/5}},$$

and with $T = 34°\text{C}$ and $Q_T = 5$.

The A-type potassium conductance at the distal dendrites greater than 100 μm away from the soma is similar to the A-type potassium conductance at the proximal dendrites except that

$$\beta_k = e^{\frac{4.53\zeta(V+1)}{273.16+T}}, \quad \zeta = -1.8 - \frac{1}{1+e^{(V+40)/5}}.$$

The hyperpolarization-activated conductance takes the form of $g_h = f_h z$, where

$$\frac{dz}{dt} = \frac{z_\infty - z}{\tau_z}, \quad z_\infty = \frac{1}{1+e^{(V+75)/8}}, \quad \tau_z = \frac{\beta_z(V)}{0.011[1+\alpha_z(V)]Q_T},$$

with

$$\alpha_z(V) = e^{0.0832(V+75)}, \quad \beta_z = e^{0.0333(V+75)},$$

and $T = 34°\text{C}$ and $Q_T = 1.16$.

The realistic neuron model also contains AMPA and GABA_A receptors, with kinetic properties described previously [16–18]. The synaptic conductance dynamics of AMPA and GABA_A are identical to those in the passive cable neuron model

$$\frac{dR}{dt} = \alpha \cdot [T] \cdot (1-R) - \beta \cdot R,$$

where R is the fraction of open receptors, α and β are forward and backward rate constants for transmitter binding, and $[T]$ is the transmitter concentration. The postsynaptic current is given by $I_{\text{syn}} = g_{\text{syn}}(E_{\text{rev}} - V)$, where V is the postsynaptic potential, E_{rev} is the reversal potential, and g_{syn} is the synaptic conductance. For AMPA and GABA_A receptors,

$$g = f_{\max} \cdot R,$$

where $f_{\max}$ is the maximum amplitude of synaptic conductance.

2.3 Model parameters

In the realistic neuron model, the parameters used in the AMPA and GABA_A receptors are largely the same as those in the previous reports [16–18, 54], with minor adjustments to match a previous iontophoretic experiment [24]. Sodium channels are distributed with a largely constant density (per unit area of membrane) along the somatodendritic axis [47]. The A-type potassium channels differ in their kinetics between the proximal and distal populations, and their density increases progressively by more than sixfold from the soma to a distance of 350 μm along the apical trunk [27,50]. The density of hyperpolarization-activated cationic current I_h also increases by more than sixfold from the soma to the distal dendrites [44]. The

distribution of AMPA receptors is set with a gradient along the dendrite to achieve a distance-dependent scaling property [1,46,52,73].

Based upon the previous experimental results, the parameters used in the realistic neuron model are set as follows: the peak conductance $f_{Na} = 30$ mS/cm^2; $f_{Kd} = 5$ mS/cm^2; $f^p_{K_A}(x) = f^{p_0}_{K_A} \cdot (1 + x/70)$, where $f^{p_0}_{K_A} = 5$ mS/cm^2, if the distance from the soma $x \le 100$ μm; $f^d_{K_A}(x) = f^{d_0}_{K_A} \cdot (1 + x/70)$ if 100 μm $< x \le 350$ μm; and $f^d_{K_A}(x) = 6.5 \cdot f^{d_0}_{K_A}$ if $x > 350$ μm, where $f^{d_0}_{K_A} = 5$ mS/cm^2; $f_h(x) = f_{h_0} + 9 \cdot f_{h_0}/[1.0 + e^{(300-x)/50}]$, where $f_{h_0} = 20$ μS/cm^2. Reversal potentials are set as: $E_{Na} = +55$ mV, $E_K = -90$ mV, $E_h = -30$ mV.

In both the passive cable model and the realistic neuron model, the resting membrane resistance r_m is set to be nonuniform along the dendritic tree [79]. The passive biophysical properties include:

$$g_L = 1/r_m,\ r_m = r_{m_0} + (r_{m_1} - r_{m_0})/[1.0 + e^{-(x-300)/50}],$$
$$\text{where } r_{m_0} = 60\ \text{k}\Omega \cdot \text{cm}^2 \text{ and } r_{m_1} = 20\ \text{k}\Omega \cdot \text{cm}^2;$$

the axial resistance $r_i = 80\ \Omega \cdot$ cm, and the capacitance $c_i = 1$ μF/cm^2. The resting membrane potential is -70 mV. The parameters of synaptic conductances are set as follows. For excitatory synapse AMPA, $\alpha = 10$ ms$^{-1} \cdot$ mM^{-1}, $\beta = 0.12$ ms^{-1}, $[T] = 1$ mM, and it lasts for 1.2 ms after the transmitter starts to release. For inhibitory synapse GABA$_A$, $\alpha = 1$ ms$^{-1} \cdot$ mM^{-1}, $\beta = 0.02$ ms^{-1}, $[T] = 1$ mM, and it lasts for 1 ms after the transmitter starts to release. Synaptic reversal potentials are $\varepsilon_E = E_{\text{AMPA}} = 0$ mV, $\varepsilon_I = E_{\text{GABA}_A} = -80$ mV.

Note that the decay time constants of AMPA and GABA$_A$ are set to be slower than typical values measured in vivo experiments, as here they are chosen mainly to fit the EPSPs and IPSPs observed in previous rat hippocampal slice experiments performed in our collaborators' lab [24, 40], in which the EPSPs and IPSPs are induced by microiontophoretic applications of glutamate and GABA at the apical dendrite. However, our conclusions are insensitive to synaptic time scales based on our analysis and numerical simulations.

2.4 Model properties

With the parameters chosen in Section 2.3, the realistic neuron model represents a rat hippocampal CA1 pyramidal neuron. The physical length of the dendrites can be as long as 900 μm, measured between the soma and the apical dendritic tufts. The electrical properties of the neuron model can be characterized by the degree of voltage attenuation from one location to another. As shown in Figure 2.2A–C, the log attenuation factor between a dendritic site and the soma, which is defined as the natural logarithm of voltage attenuation from the dendritic site to the soma [29,86], can be as large as 4 near the resting state measured by constant current drive, and it can increase to 5 and 7 when 10 Hz and 50 Hz sinusoidal current inputs are given respectively, reflecting the dendritic property of low pass filter. To be intuitive,

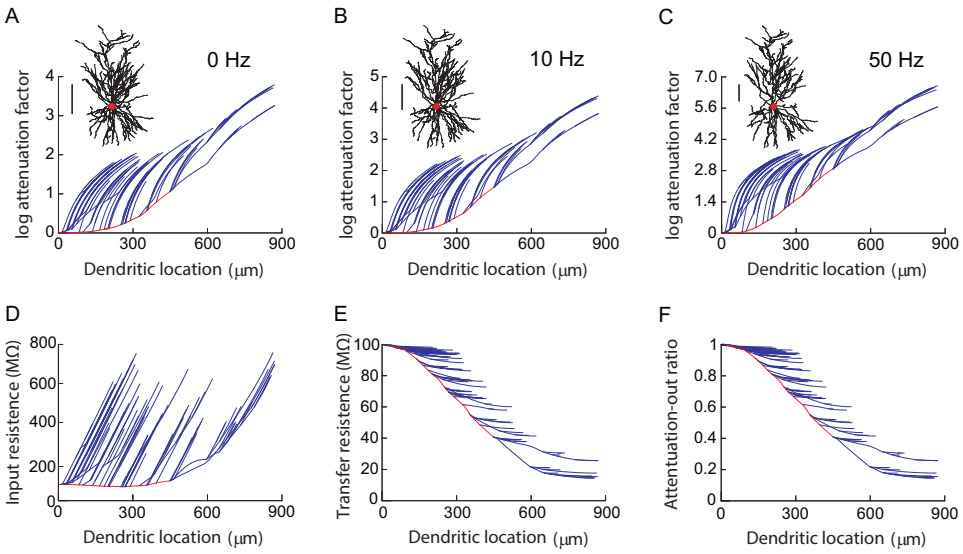

FIGURE 2.2. The electrical property of the realistic neuron model. (A)–(C), the voltage attenuation between all dendritic sites and the soma under constant, 10 Hz, and 50 Hz sinusoidal current input drive on each dendritic site. The log attenuation factor between a dendritic site and the soma is defined as the logarithm of voltage attenuation from the dendritic site to the soma. Inset in (A)–(C) is the electrotonic architecture of the neuron in which the distance between any two locations is represented by the log attenuation factor between them. Scale bar represents one log unit of attenuation, i.e. the distance that signifies an e-fold decay of voltage. (D) The input resistance at different dendritic locations. (E) The transfer resistance at different dendritic locations. The transfer resistance is defined as the ratio of local dendritic voltage change to the current injection at the soma. (F) The attenuation-out ratio at different dendritic locations. The attenuation-out ratio is defined as the ratio of local dendritic voltage change to the somatic voltage change when injecting current at the soma. In (A)–(F), each line corresponds to either the dendritic trunk (red) or a dendritic branch (blue).

the electrotonic architecture of the dendrites is also shown in the inset of Figure 2.2(A)–(C). The electrotonic length of the dendrites is 4 as measured between the soma and the apical tufts.

The input resistance at the soma is about 100 MΩ, and the input resistance at the dendritic tips can be as high as 775 MΩ, as shown in Figure 2.2(D). In addition, the transfer resistance, measured as the ratio of local dendritic voltage change to the current injection at the soma, ranges from about 100 MΩ at proximal dendrites near the soma to about 15 MΩ at distal dendrites, as shown in Figure 2.2(E). Furthermore, the voltage attenuation-out ratio, measured as the ratio of

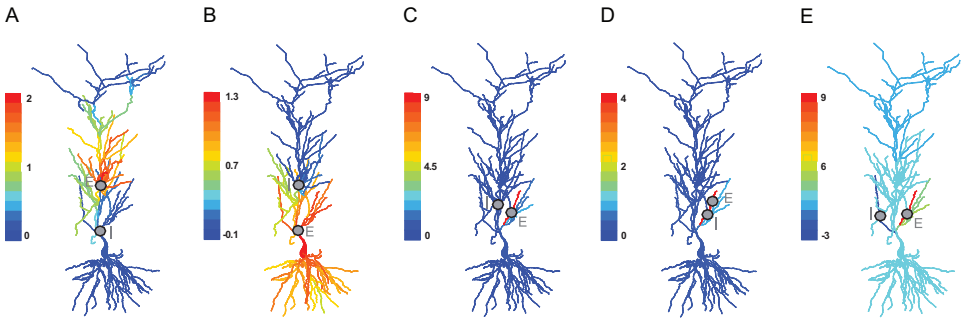

FIGURE 2.3. Spatial profile of membrane potentials on the whole dendrites when the realistic neuron model receives a pair of E and I inputs simultaneously. Input locations are marked by gray dots in each panel. Membrane potential is coded by color in the unit of mV. (A), E and I inputs on the dendritic trunk, the I input is more proximal to the soma than the E input. (B), E and I inputs on the dendritic trunk, the I input is more distal to the soma than the E input. (C), I input on the dendritic trunk, and E input on a dendritic branch. (D), E and I inputs on the same dendritic branch. (E), E and I inputs on two different branches. All membrane potential values are measured at the time 5 ms after the inputs are received.

local dendritic voltage change to the somatic voltage change when injecting current at the soma, reduces from 100% at proximal dendrites near the soma to 15% at distal dendrites, as shown in Figure 2.2(F). By injecting step currents into the soma, the membrane time constant of the realistic neuron model is estimated to be 10 ms.

The NEURON software [9] is used as a numerical solver to compute both the passive and the active models with the numerical scheme of Crank-Nicolson and with a time step of 0.1 ms. As an example shown in Figure 2.3, when the realistic neuron model receives a pair of E and I inputs on different dendritic locations, we can simulate the model numerically to obtain its membrane potential change across the whole dendrites. In particular, we are interested in how the neuron integrates synaptic inputs and changes its membrane potential at the soma, which will be investigated in details below. The simulation code is available at `https://github.com/songting858/dendritic_integration`.

3 Integration Rules of Synaptic Inputs

In this section, the summation rules of synaptic inputs are studied via the mathematical analysis of the cable neuron model, along with the numerical computation of the realistic neuron model. The integration rule for a pair of E and I synaptic inputs is first investigated in Section 3.1 and Section 3.2. The characterization of the integration of multiple E and I synaptic inputs is then generalized in Section 3.3.

3.1 A pair of *E* and *I* synaptic inputs

It is noticed that the cable neuron model (equations (2.6)-(2.10)) is mathematically solvable when the synaptic input I_{syn} is replaced with an injected current input I_{inj}. In such a case, the cable equation

$$c_i \frac{\partial v_i}{\partial t} = -g_{Li} v_i + I_{\text{inj}} + \frac{d_i}{4r_i} \frac{\partial^2 v_i}{\partial x^2}$$

with the boundary conditions (equations (2.7)-(2.10)) is a linear system. Therefore, its Green's function $\Gamma(\boldsymbol{x}, \boldsymbol{y}, t)$ in response to a delta-impulse current input at location $\boldsymbol{y}$ and at time $t = 0$ exists in principle. Accordingly, the solution of the neuronal response can be solved as $v(\boldsymbol{x}, t) = \Gamma \star I_{\text{inj}}$, where $\star$ denotes convolution in both space and time. However, in contrast to the injected current, the synaptic current in equation (2.1) includes the unknown dynamical variable v_i. Therefore, the neuronal response v_i depends nonlinearly on the synaptic current inputs, and this Green's function method cannot be directly applied to obtain an analytical solution of equation (2.6) driven by synaptic current inputs. We adopt a regular perturbation method to develop an analytical representation for the synaptic input case. The solution of an unbranched cable neuron model with conductance-based synaptic inputs (equations (2.11)–(2.13)) has been obtained recently [40], but the solution of the branched cable neuron model (equations (2.6)–(2.10)) has not been obtained yet. Below we derive the solution of the branched cable neuron model.

When a neuron receives an E input or an I input alone, one can measure the corresponding EPSP trace or IPSP trace at the soma. It shall be clarified that, unless stated otherwise, the terms of EPSP and IPSP throughout the article refer to postsynaptic membrane potentials at the soma rather than those at a local dendritic site. Note that, within the physiological regime, i.e., the amplitude of an EPSP being less than 6 mV and the amplitude of an IPSP being less than 3 mV, the corresponding input strengths f_E and f_I are relatively small. Therefore, given both an E input at $\boldsymbol{x_E} = (i_E, x_E)$ and an I input at $\boldsymbol{x_I} = (i_I, x_I)$, the membrane potential response $v(\boldsymbol{x}, t)$ can be represented as a series in the powers of f_E and f_I,

$$v(\boldsymbol{x}, t; \mathcal{W}) = \sum_{k=0}^{\infty} \sum_{m+n=k} f_E^m f_I^n v_{mn}(\boldsymbol{x}, t; \mathcal{W}), \tag{3.1}$$

where $\mathcal{W} \subseteq \{\boldsymbol{x_E}, \boldsymbol{x_I}, t_E, t_I\}$ is the parameter space, $\boldsymbol{x_E}, t_E \in \mathcal{W}$ if $m \neq 0$; $\boldsymbol{x_I}, t_I \in \mathcal{W}$ if $n \neq 0$. The parameters are omitted sometimes if self-evident. In addition, for each dendritic segment i, by switching the global coordinate representation to the local coordinate representation, one has

$$v_{mn}(\boldsymbol{x}, t; \mathcal{W}) = v_{i_{mn}}(x, t; \mathcal{W}) \tag{3.2}$$

for any $\boldsymbol{x} = (i, x)$. Combining equations (3.1)–(3.2) and the cable equation (equation (2.6)), order by order, one can obtain a hierarchy of differential equations for

each segment i. For the zeroth order, one has

$$c_i \frac{\partial v_{i_{00}}}{\partial t} = -g_{Li} v_{i_{00}} + \frac{d_i}{4r_i} \frac{\partial^2 v_{i_{00}}}{\partial x^2}.$$

Using the initial condition $v_i(x, 0) = 0$, the solution is simply $v_{i_{00}}(x, t; \varnothing) = 0$, or

$$v_{00}(\boldsymbol{x}, t; \varnothing) = 0 \tag{3.3}$$

for $\boldsymbol{x}$ on any segment of the neuron. This solution can be interpreted as that a neuron remains to stay at its resting state in the absence of any zeroth-order input. For the first order of excitation $\mathcal{O}(f_E)$, one has

$$c_i \frac{\partial v_{i_{10}}}{\partial t} = -g_{Li} v_{i_{10}} + \frac{d_i}{4r_i} \frac{\partial^2 v_{i_{10}}}{\partial x^2} - u_E(t; t_E)\delta(\boldsymbol{x} - \boldsymbol{x_E})(v_{i_{00}} - \varepsilon_E).$$

With the help of the Green's function, the solution can be explicitly expressed as

$$v_{10}(\boldsymbol{x}, t; \boldsymbol{x_E}, t_E) = \Gamma(\boldsymbol{x}, \boldsymbol{x_E}, t) * [u_E(t; t_E)(\varepsilon_E - v_{00}(\boldsymbol{x_E}, t; \varnothing))]. \tag{3.4}$$

Here '$*$' denotes convolution in time, $\Gamma(\boldsymbol{x}, \boldsymbol{y}, t)$ is the Green's function of the system that is obtained by injecting a δ-pulse input as discussed previously, and $v_{00}(\boldsymbol{x_E}, t; \varnothing) = 0$ is given by equation (3.3). This solution can be interpreted as that, when the local membrane potential is maintained at the resting state v_{00}, the neuron changes its membrane potential to the first-order correction $f_E v_{10}$ in response to the synaptic current $g_E(\varepsilon_E - v_{00})$ at $\boldsymbol{x_E}$. Similarly, one can have the first-order solution to the I input $\mathcal{O}(f_I)$,

$$v_{01}(\boldsymbol{x}, t; \boldsymbol{x_I}, t_I) = \Gamma(\boldsymbol{x}, \boldsymbol{x_I}, t) * [u_I(t; t_I)(\varepsilon_I - v_{00}(\boldsymbol{x_I}, t; \varnothing))]. \tag{3.5}$$

For the second-order of excitation $\mathcal{O}(f_E^2)$, one has

$$c_i \frac{\partial v_{i_{20}}}{\partial t} = -g_{Li} v_{i_{20}} + \frac{d_i}{4r_i} \frac{\partial^2 v_{i_{20}}}{\partial x^2} - u_E(t; t_E)\delta(\boldsymbol{x} - \boldsymbol{x_E}) v_{i_{10}}. \tag{3.6}$$

Because v_{10} is already given by equation (3.4), the solution of equation (3.6) can be explicitly expressed as

$$v_{20}(\boldsymbol{x}, t; \boldsymbol{x_E}, t_E) = \Gamma(\boldsymbol{x}, \boldsymbol{x_E}, t) * [-u_E(t; t_E) v_{10}(\boldsymbol{x_E}, t; \boldsymbol{x_E}, t_E)]. \tag{3.7}$$

This solution can be interpreted as that, when the local membrane potential is maintained at the first-order correction $f_E v_{10}$, the neuron changes its membrane potential to the second-order correction $f_E^2 v_{20}$ in response to the synaptic current $-g_E f_E v_{10}$ at $\boldsymbol{x_E}$. Similarly, one can have the second-order solution to the I input $\mathcal{O}(f_I^2)$,

$$v_{02}(\boldsymbol{x}, t; \boldsymbol{x_I}, t_I) = \Gamma(\boldsymbol{x}, \boldsymbol{x_I}, t) * [-u_I(t; t_I) v_{01}(\boldsymbol{x_I}, t; \boldsymbol{x_I}, t_I)]. \tag{3.8}$$

For the order of $\mathcal{O}(f_E f_I)$, one has

$$\begin{aligned} c_i \frac{\partial v_{i_{11}}}{\partial t} = &-g_{Li} v_{i_{11}} + \frac{d_i}{4r_i} \frac{\partial^2 v_{i_{11}}}{\partial x^2} - u_E(t; t_E)(t)\delta(\boldsymbol{x} - \boldsymbol{x_E}) v_{i_{01}} \\ &- u_I(t; t_I)\delta(\boldsymbol{x} - \boldsymbol{x_I}) v_{i_{10}}, \end{aligned} \tag{3.9}$$

whose solution is obtained as

$$
\begin{aligned}
&v_{11}(\boldsymbol{x}, t; \boldsymbol{x_E}, \boldsymbol{x_I}, t_E, t_I) \\
&\quad = \Gamma(\boldsymbol{x}, \boldsymbol{x_E}, t) * [-u_E(t; t_E) v_{01}(\boldsymbol{x_E}, t; \boldsymbol{x_I}, t_I)] \\
&\qquad + \Gamma(\boldsymbol{x}, \boldsymbol{x_I}, t) * [-u_I(t; t_I) v_{10}(\boldsymbol{x_I}, t; \boldsymbol{x_E}, t_E)].
\end{aligned} \tag{3.10}
$$

The above procedure and physical interpretation can be generalized to higher orders.

All these analytical solutions involve the Green's function of the system in reponse to a δ-pulse input as discussed previously. The Green's function of the ball-and-stick model (equations (2.11)–(2.13)) has been solved previously [40, 41, 82]. However, the Green's function of a branched cable model is difficult to obtain analytically. Fortunately, it can be efficiently measured numerically using white-noise input [5], i.e.,

$$\Gamma(\boldsymbol{x}, \boldsymbol{y}, \tau) = \langle v(\boldsymbol{x}, t) I^w_{\text{inj}}(\boldsymbol{y}, t - \tau) \rangle,$$

where $I^w_{\text{inj}}(\boldsymbol{y}, t)$ is the standard white noise with unitary variance injected at location $\boldsymbol{y}$, $v(\boldsymbol{x}, t)$ is the corresponding response measured at location $\boldsymbol{x}$, and $\langle \cdot \rangle$ is the temporal correlation. This method is also known as the reverse correlation method in neurophysiology [65].

The numerically measured Green's function of the cable model (equations (2.6)–(2.10)) enables one to directly evaluate the performance of the perturbation solutions in approximating the numerical solutions of the cable neuron model. When the cable neuron model receives a pair of E and I synaptic inputs either individually or jointly on the dendrites, our numerical simulation of the model using the Crank-Nicolson scheme shows that the second-order perturbation solutions are sufficiently accurate to capture the solutions of physiological membrane potentials, as demonstrated in Figure 3.1. Therefore, the EPSP at the soma denoted by V_E induced by an individual E input alone can be approximated by

$$V_E \approx f_E v_{10}(\boldsymbol{x_S}, t) + f_E^2 v_{20}(\boldsymbol{x_S}, t),$$

where $\boldsymbol{x_S}$ denotes the location of the soma. The IPSP at the soma denoted by V_I induced by an individual I input alone can be approximated by

$$V_I \approx f_I v_{01}(\boldsymbol{x_S}, t) + f_I^2 v_{02}(\boldsymbol{x_S}, t),$$

and the summed somatic potential (SSP) at the soma denoted by V_S induced by both E and I inputs can be approximated by

$$
\begin{aligned}
V_S \approx\ & f_E v_{10}(\boldsymbol{x_S}, t) + f_E^2 v_{20}(\boldsymbol{x_S}, t) + f_I v_{01}(\boldsymbol{x_S}, t) \\
& + f_I^2 v_{02}(\boldsymbol{x_S}, t) + f_E f_I v_{11}(\boldsymbol{x_S}, t).
\end{aligned}
$$

Based on the second-order perturbation solutions, we can identify a bilinear dendritic integration rule that captures the somatic membrane potential response when the neuron receives a pair of E and I inputs, i.e.,

$$V_S = V_E + V_I + \kappa_{EI} V_E V_I, \tag{3.11}$$

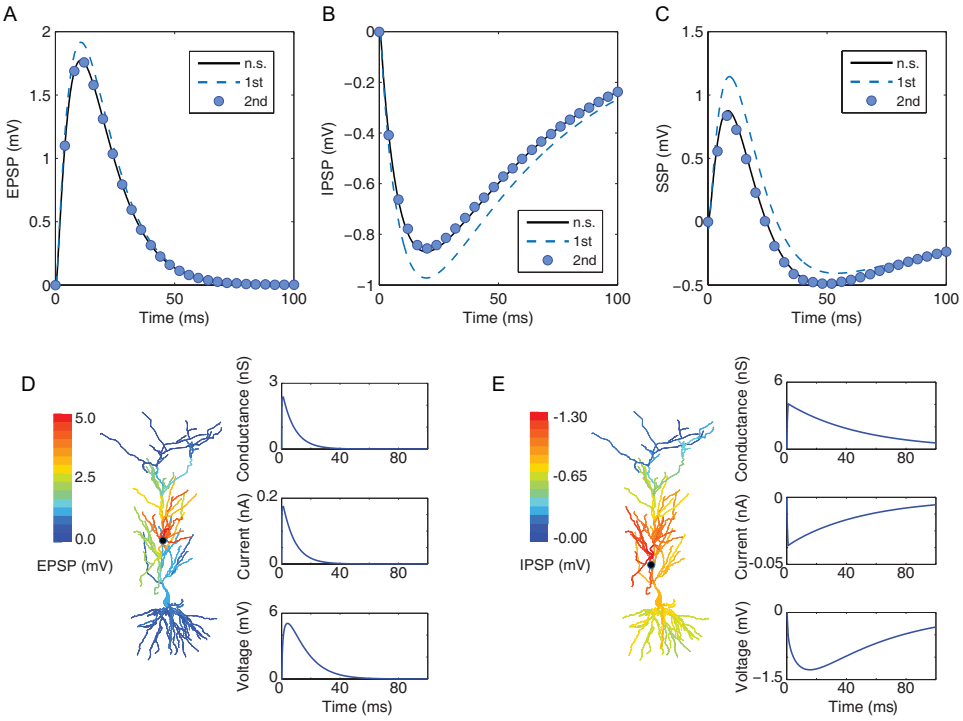

FIGURE 3.1. Analytical solutions of various orders to the cable neuron model for (A) EPSP, (B) IPSP, and (C) summed somatic potential (SSP) in comparison with numerical solutions to the cable neuron model. The dashed blue line is the first-order approximation. The blue circle is the second-order approximation. The solid black line is the numerical solution to the cable neuron model. (D) Left, color-coded membrane potential distribution across the whole dendrites when the cable neuron receives an E input on the dendritic trunk about 300 μm away from the soma. The membrane potentials are shown at the time when the response at the input site reaches its peak value. The input location is marked by a black dot. Right, local conductance, synaptic current, and membrane potential measured at the input site. The corresponding EPSP measured at the soma is shown in (A). (E), the same as (D), but for the case of an I input received on the dendritic trunk about 200 μm away from the soma. The membrane potentials on the left are shown at the time when the response at the input site reaches its trough value. The corresponding IPSP measured at the soma is shown in (B). All the membrane potentials are relative to the resting potential.

in which the coefficient κ_{EI} is defined as

$$\begin{aligned}
&\kappa_{EI}(\boldsymbol{x_S}, t; \boldsymbol{x_E}, \boldsymbol{x_I}, t_E, t_I) \\
&\quad \equiv \frac{V_S - V_E - V_I}{V_E \cdot V_I} \\
&\quad = \frac{v_{11}(\boldsymbol{x_S}, t; \boldsymbol{x_E}, \boldsymbol{x_I}, t_E, t_I)}{v_{10}(\boldsymbol{x_S}, t; \boldsymbol{x_E}, t_E) \cdot v_{01}(\boldsymbol{x_S}, t; \boldsymbol{x_I}, t_I)} + \mathcal{O}(f).
\end{aligned} \tag{3.12}$$

Here $\mathcal{O}(f) = \mathcal{O}(f_E) + \mathcal{O}(f_I)$. equation (3.12) shows that the leading order of κ_{EI} as a function of time is independent of the input strengths f_E and f_I. The variables and parameters will be omitted in the expression of κ_{EI} below as we only concern with the dendritic integration effects at the soma. In addition, equation (3.12) indicates that κ_{EI} is determined by the input locations and input arrival times. Therefore, κ_{EI} parameterizes the spatiotemporal information of synaptic inputs. The coefficient κ_{EI} measures the shunting effect of the I input. In particular, $\kappa_{EI} = 0$ corresponds to the special case of linear summation of the E and I inputs. Therefore, κ_{EI} is referred to as the shunting coefficient below. Note that κ_{EI} is a novel measure for the effect of shunting inhibition, different from previous measures such as input resistance change [22].

A special form of the bilinear integration rule equation (3.11) was first discovered in an experiment [24], which was measured at a particular time point when the EPSP reaches its peak value and the E and I synaptic inputs were received on the dendritic trunk simultaneously, and its mechanism was analyzed based on the analysis of the ball-and-stick model (equations (2.11)–(2.13)) with an unbranched dendrite [40, 41]. Here the perturbation analysis is performed on the cable neuron model with branched dendritic structure, and synaptic inputs can be elicited on any dendritic site of the neuron. The analysis further generalizes the rule to the case of a pair of unsimultaneous synaptic inputs and the generalized rule holds at any time moment. Note that the bilinear integration rule (equation (3.11)) holds at any locations on the neuron, including its soma in particular.

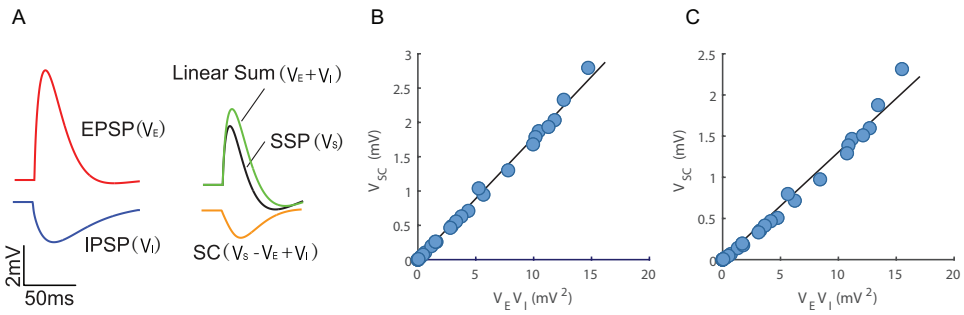

FIGURE 3.2. Dendritic integration of a pair of E and I inputs on the dendritic trunk in the realistic neuron model. (A) A set of EPSP, IPSP, and SSP measured in the realistic neuron model. The linear sum and SC are calculated correspondingly. (B) The bilinear relation between the SC and the product of the EPSP and the IPSP at the peak time of EPSP when the EPSP and the IPSP are induced simultaneously. Each blue dot corresponds to a set of EPSP, IPSP, and SSP. The black line is linear fitting. The E and I inputs are given on the dendritic trunk about 311 μm and 268 μm away from the soma, respectively. (C) The same as (B) except that the EPSP is induced 20 ms later than the IPSP.

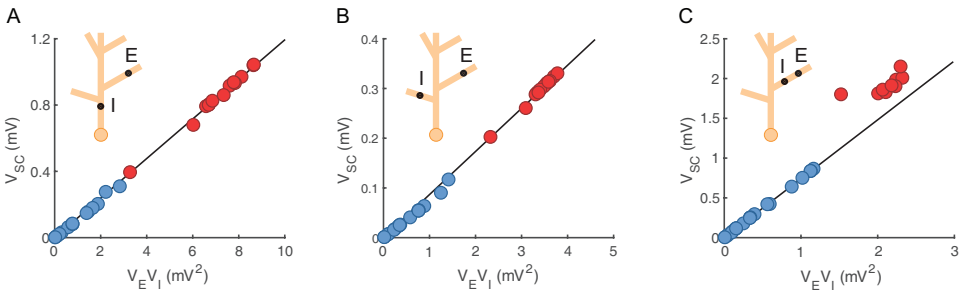

FIGURE 3.3. Dendritic integration of a pair of E and I inputs on dendritic branches in the realistic neuron model. (A) E on a dendritic branch and I on the dendritic trunk. (B) E and I on two separate dendritic branches. (C) E and I on the same dendritic branch. In (A)–(C), inset shows the input configuration. Blue and red dots correspond to small and large strengths of E inputs triggering subthreshold dendritic EPSP and dendritic spikes, respectively. The black line is linear fitting.

As the rule is derived from the passive cable model, it is necessary to further validate the rule in realistic neuron simulations in which active channels are taken into account in the model. The details of the realistic neuron model and the related computational method can be found in Section 2.2 and Section 2.3. The numerical computation results are summarized below. As shown in Figure 3.2(A), when the E and I inputs are elicited concurrently (i.e., $t_E = t_I$) at two different locations on the dendritic trunk, the SSP is found to be always smaller than the linear sum of the EPSP and the IPSP when elicited separately. The difference between the SSP and the linear sum of the EPSP and the IPSP is referred to as the shunting component (SC). The amplitude of the EPSP and the IPSP is then varied by randomly choosing the input strengths f_E and f_I. To be consistent with experimental observations [24], the amplitude of the EPSP is set to range between 0 mV and 6 mV, and the amplitude of the IPSP is set to range between 0 mV and -3 mV. For a pair of fixed input strengths f_E and f_I, the set of time courses of the EPSP, the IPSP, and the corresponding SSP is obtained. Using 30 sets of such data with different input strengths, the amplitude of the SC is found to depend linearly on the product of the EPSP and IPSP amplitudes at any time point. A special case of the time when the EPSP reaches its peak value is shown in Figure 3.2(B), in which the excellent linear fitting shows that the slope κ_{EI} is independent of the amplitudes of the EPSP and the IPSP. This reproduces the experimental observation [24]. For the case of nonconcurrent E and I inputs (i.e., $t_E \neq t_I$), when the onset of the I input is 20 ms earlier than that of the E input, our numerical results show that the bilinear integration rule (equation (3.11)) still holds in Figure 3.2(C).

The validity of the bilinear integration rule is also investigated for E and I inputs randomly distributed on dendritic branches in the realistic neuron model. As shown in Figure 3.3, when the E input on a branch does not trigger a dendritic spike, the

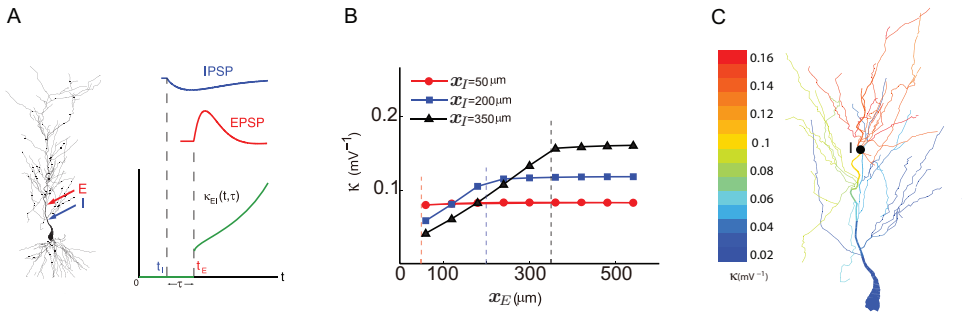

FIGURE 3.4. Spatiotemporal dependence of κ_{EI} in the realistic neuron model for inputs on the dendritic trunk. (A) Left, the locations of a pair of E and I inputs indicated by arrows. The time difference between the E and I inputs is $\tau = 20$ ms. Right, (upper) the temporal profiles of an EPSP (solid red line) and an IPSP (solid blue line). The arrival times of the EPSP and the IPSP indicated by vertical dashed lines; (lower) the temporal profile of the shunting coefficient κ_{EI} indicated by the solid green line. (B)–(C), spatial asymmetry of the shunting coefficient κ_{EI}. (B) κ_{EI} as a function of distance between the E input location and the soma for three fixed I input locations at the dendritic trunk about 50 μm, 200 μm, and 350 μm away from the soma, respectively, which are marked by colored vertical lines. (C) κ_{EI} for an I input (black dot) fixed at the apical trunk, with an E input scanned throughout part of the apical dendrites of the realistic neuron model with length less than 550 μm. The value of κ_{EI} is coded in color.

rule holds for I inputs located either on the dendritic trunk or on dendritic branches. In addition, when the E input on a branch is strong enough to trigger a dendritic spike, the bilinear rule remains valid when the I input is located on the dendritic trunk or on a different branch from the E input. In such input configurations, despite the large amplitude of a dendritic spike at the E input site, our simulation indicates that the amplitude of membrane potential attenuates to a small value at the I input site, resulting in the validity of the bilinear integration rule. The bilinear rule breaks down when the interaction between the E and I inputs is too strong to be captured by the second-order perturbation method, e.g., when a dendritic spike is generated near the I input location as shown in Figure 3.3(C).

3.2 Spatiotemporal dependence of κ_{EI}

For a fixed pair of E and I input locations, κ_{EI} is a function of both time t and the arrival time difference between the E and I input $\tau = t_E - t_I$, as illustrated in Figure 3.4(A). Qualitatively, when the I input arrives earlier than the E input, i.e., $t_I < t_E$, the shunting coefficient κ_{EI} remains at zero until the EPSP arrives at t_E. In addition, when t or τ becomes large, the SC tends to vanish because V_E or V_I or both of them will approach zero. In such a case, the bilinear integration

becomes insensitive to the shunting coefficient κ_{EI}, thus κ_{EI} can be set to an arbitrary number of order one or simply set to zero without much influence on the change of SSP.

For a fixed time point, κ_{EI} is a function of input locations. By fixing the location of the I input $\boldsymbol{x_I}$, the spatial dependence of the shunting coefficient κ_{EI} on the E input $\boldsymbol{x_E}$ can be theoretically analyzed. In such a case, $v_{01}(\boldsymbol{x_S}, t; \boldsymbol{x_I}, t_I)$ in equation (3.12) is fixed. In addition, note that v_{11} in equation (3.10) can be further simplified by ignoring the first term due to the fact that $|\varepsilon_E \gg |\varepsilon_I|$, as a typical value of $\varepsilon_E = 70$ mV and $\varepsilon_I = -10$ mV with respect to the resting potential. Accordingly,

$$v_{11}(\boldsymbol{x}, t) \approx \Gamma(\boldsymbol{x}, \boldsymbol{x_I}, t) * [-u_I(t; t_I) v_{10}(\boldsymbol{x_I}, t; \boldsymbol{x_E}, t_E)]; \tag{3.13}$$

equation (3.13) indicates that the SC mainly originates from the correction of IPSP by the outward synaptic current induced by the first-order EPSP measured at site $\boldsymbol{x_I}$. By using equations (3.12)–(3.13), the shunting coefficient κ_{EI} can be expressed as

$$\kappa_{EI} \propto \frac{\Gamma(\boldsymbol{x_S}, \boldsymbol{x_I}, t) * [-u_I(t) v_{10}(\boldsymbol{x_I}, t; \boldsymbol{x_E}, t_E)]}{v_{10}(\boldsymbol{x_S}, t; \boldsymbol{x_E}, t_E)}, \tag{3.14}$$

where $\propto$ is the proportional symbol. A spatial asymmetry property of κ_{EI} can be analytically obtained from equation (3.14); namely, the value of k_{EI} shows an asymmetry in its dependence on E and I input locations. The spatial asymmetry property of κ_{EI} is valid for synaptic inputs distributed on branched dendrites. For the ease of illustration, here the unbranched ball-and-stick neuron model is first analyzed. The Green's function of the ball-and-stick model has been obtained as [40, 41, 82]:

$$\Gamma(x, y, t) = \sum_{n=0}^{\infty} H_n(x, y) e^{-\frac{k_n}{c} t}, \tag{3.15}$$

where

$$H_n(x, y) = \sqrt{\frac{r}{c^2 d}} \cdot \frac{4\gamma \cos[w_n(1 - x/l)] \cos[w_n(1 - y/l)]}{\gamma\lambda + \gamma\lambda w_n^{-1} \sin(w_n) \cos(w_n) + 2\cos^2(w_n)},$$

$\gamma = (\pi d^2/2S)(rd)^{-1/2}$, $\lambda = l\sqrt{4r/d}$, and w_n and k_n are solved from $w_n = -i\sqrt{-k_n + g_L}\lambda$, $\tan(w_n) = -\frac{w_n}{\gamma\lambda}$.

In the small limit of the dendritic length l, one has $w_0 = 0$, $w_n \approx (n - \frac{1}{2})\pi$ for $n \geq 1$, which corresponds to $k_0 = g_L$, $k_n \approx \alpha w_n^2/l^2$ for $n \geq 1$ with $\alpha = d/4r$. Accordingly, by using equations (3.4) and (3.15) in the limiting case, one

can obtain the following approximation for $v_{10}(x_I, t; x_E, t_E = 0)$,

$$
\begin{aligned}
v_{10} \approx\ & \frac{\beta}{1+\gamma l} e^{-g_L t/c} * g_E \\
& + \frac{2\beta c l g_E}{\alpha\gamma} \sum_{n=1}^{\infty} \frac{1}{w_n^2} \cos\Big[w_n\Big(1-\frac{x_I}{l}\Big)\Big] \cos\Big[w_n\Big(1-\frac{x_E}{l}\Big)\Big],
\end{aligned}
\tag{3.16}
$$

where $\beta = \gamma\varepsilon_E\big(4r/c^2 d\big)^{1/2}$. One can further approximate

$$\partial_{x_E}^2 v_{10}(x_I, t; x_E, t_E = 0)$$

as

$$\frac{\partial^2 v_{10}}{\partial x_E^2} \approx \frac{\beta c g_E}{\alpha\gamma l}\left[\delta_c\Big(\frac{x_I+x_E}{2l}\Big) - \delta_c\Big(\frac{x_I+x_E}{l}\Big) - \delta_c\Big(\frac{x_I-x_E}{2l}\Big) + \delta_c\Big(\frac{x_I-x_E}{l}\Big)\right],$$

where $\delta_c(\cdot)$ is the Dirac comb with period 2. Note that there is only one single delta function at $x_E = x_I$ with a negative sign for $x_{E,I} \in [0, l]$, which means $\partial_{x_E} v_{10}(x_I, t; x_E, t_E = 0)$ is a step function of x_E. From equation (3.16), one has $\partial_{x_E} v_{10}(x_I, t; x_E, t_E = 0) = 0$ at $x_E = l$. Thus, $\partial_{x_E} v_{10}(x_I, t; x_E, t_E = 0)$ is a positive constant for $x_E \in [0, x_I]$ and vanishes for $x_E \in [x_I, l]$. Therefore, $v_{10}(x_I, t; x_E, t_E = 0)$ is a piecewise linear function, increasing for x_E between the soma and x_I, whereas being constant when x_E exceeds x_I. Similarly, one can further show that $v_{10}(x_S, t; x_E, t_E = 0)$ is a constant when $x_E \in [0, l]$. Combining these facts in equation (3.14) leads to the spatial asymmetry of k_{EI} in the small l limit; i.e., for each I input location, the dependence of κ_{EI} on the E input location shows a clear asymmetry for proximal E input versus distal E input—k_{EI} decays with the distance between E and I inputs closer to the soma than the I input, while it remains constant for E inputs more distal to the soma than the I input.

Intuitively, the spatial asymmetry property of κ_{EI} for inputs on the dendritic trunk can be understood through the following argument of equation (3.14). As $\boldsymbol{x_I}$ is fixed, $\Gamma(\boldsymbol{x_S}, \boldsymbol{x_I}, t)$ is determined. When $\boldsymbol{x_E}$ is on the path between the soma and $\boldsymbol{x_I}$, given an E input at $\boldsymbol{x_E}$, the membrane potential response measured at the soma as $v_{10}(\boldsymbol{x_S}, t; \boldsymbol{x_E}, t_E)$ and measured at $\boldsymbol{x_I}$ as $v_{10}(\boldsymbol{x_I}, t; \boldsymbol{x_E}, t_E)$ are smaller than the local membrane potential measured at $\boldsymbol{x_E}$ as $v_{10}(\boldsymbol{x_E}, t; \boldsymbol{x_E}, t_E)$ due to the current leak along the current propagation path. As $\boldsymbol{x_E}$ approaches $\boldsymbol{x_I}$, $v_{10}(\boldsymbol{x_S}, t; \boldsymbol{x_E}, t_E)$ decreases due to the larger current leak on the way from $\boldsymbol{x_E}$ to the soma. On the contrary, $v_{10}(\boldsymbol{x_I}, t; \boldsymbol{x_E}, t_E)$ increases due to the smaller current leak on the way from $\boldsymbol{x_E}$ to $\boldsymbol{x_I}$. Therefore, κ_{EI} increases as $\boldsymbol{x_E}$ gets closer to $\boldsymbol{x_I}$ when $\boldsymbol{x_E}$ is between the soma and $\boldsymbol{x_I}$. When $\boldsymbol{x_E}$ is further away from the soma than $\boldsymbol{x_I}$, both $v_{10}(\boldsymbol{x_S}, t; \boldsymbol{x_E}, t_E)$ and $v_{10}(\boldsymbol{x_I}, t; \boldsymbol{x_E}, t_E)$ start to decrease when $\boldsymbol{x_E}$ gets further. However, the decrease of the numerator and denominator in equation (3.14) almost cancel out, which leads to the constant κ_{EI}. The spatial dependence of the shunting coefficient κ_{EI} indicates a uniformly high shunting efficacy for all

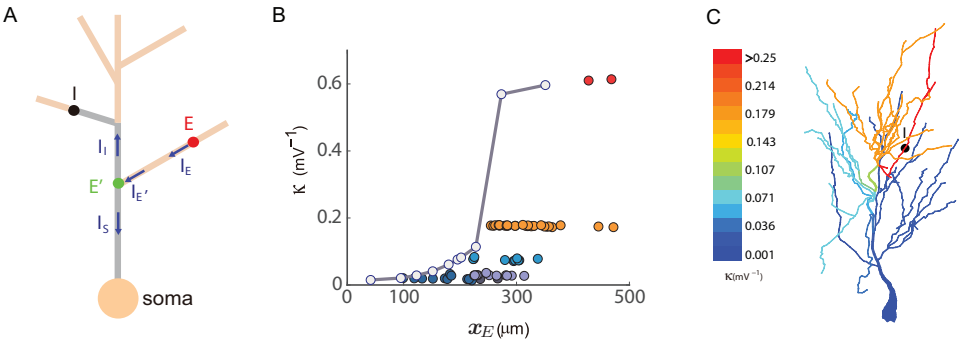

FIGURE 3.5. Spatial dependence of κ_{EI} in the realistic neuron model for inputs on the dendritic branch. (A) A schematic branched dendrite. Gray color denotes the I path defined as the path from the I input site to the soma. (B) Spatial profile of κ_{EI} as a function of the E input location distributed on part of the dendrites. E inputs located on the same branch connecting to the I path are marked by dots with the same color. E inputs located on the I path are marked by gray and connected by gray line. (C) κ_{EI} for an I input (black dot) fixed at a dendritic branch, with an E input scanned throughout part of the apical dendrites of the realistic neuron model with length less than 550 μm. The value of κ_{EI} is coded in color.

E inputs that are more distal than the I input, supporting the on-the-path theory [34] that inhibition is most effective when the I input is on the direct path from the E input to the soma.

The property of spatial asymmetry of κ_{EI} is more general than the case of the passive ball-and-stick neuron. It has been shown that the ball-and-stick neuron model is mathematically equivalent to a large class of neurons with branched dendrites [56]. Therefore, the spatial asymmetry property of κ_{EI} remains valid for neurons in this class. In addition, as shown in Figure 3.4(B)–(C), when the E and I inputs are on the dendritic trunk, the spatial asymmetry property of κ_{EI} is validated through our numerical computation of the realistic neuron model which is a representative of a wide range of neuron class.

When a pair of E and I inputs are located on dendritic branches, the analysis of the cable neuron model further predicts the spatial dependence of κ_{EI} below. As shown in Figure 3.5(A), for a fixed I input location (marked by the black dot in Figure 3.5(A), the I path (marked by gray) is defined as the path between the soma and the I input. Along the I path, κ_{EI} increases as the E input moves away from the soma towards the I input, similar to the previous case where the inputs are on the dendritic trunk. For each branch connecting to the I path, κ_{EI} is predicted to be constant for all E sites on the branch. This can be seen as follows. According to equation (3.14), κ_{EI} depends on $v_{10}(0,t;x_E)$ and $v_{10}(x_I,t;x_E)$ for a fixed I site. For an arbitrary E site (say, marked by the red dot in Figure 3.5(A) on a

branch, during the evolution of $v_{10}(x,t;x_E)$, an axial current $\mathrm{I_E}$ is initiated by the input current $\varepsilon_E g_E(t)$ at the E site (equation (3.4)) and then flows to the remaining part of the neuron. The axial current decays to $\mathrm{I_{E'}}$ at the branching point E' (marked by the green dot in Figure 3.5(A). At E', $\mathrm{I_{E'}}$ splits into a flow towards the soma denoted by $\mathrm{I_S}$ and a flow towards the I site denoted by $\mathrm{I_I}$. If we shift the stimulus location E to E' with a new input conductance at E' so as to keep $\mathrm{I_{E'}}$ unchanged, then the flows $\mathrm{I_S}$ and $\mathrm{I_I}$ remain the same. Therefore, after the stimulus site shifted, the membrane potential measured at the soma $v_{10}(0,t;x_E)$ and the I site $v_{10}(x_I,t;x_E)$ remains unchanged. Since any E site on a branch can be equivalently shifted to the E' site with certain input strength, while the shunting coefficient is independent of the input strength, we have the same value of κ_{EI} at any site on a branch connecting to the same branching point. The prediction of the spatial dependence of κ_{EI} for inputs on dendritic branches is verified in our realistic neuron simulations in Figure 3.5(B)–(C).

3.3 Multiple synaptic inputs

Based on a similar analysis, it is straightforward to generalize equation (3.11) to describe the dendritic integration of a pair of E inputs as

$$V_S = V_{E_1} + V_{E_2} + \kappa_{E_1E_2} V_{E_1} V_{E_2},$$

and the dendritic integration of a pair of I inputs as

$$V_S = V_{I_1} + V_{I_2} + \kappa_{I_1I_2} V_{I_1} V_{I_2},$$

and the dendritic integration of multiple E and I synaptic inputs as

$$\begin{aligned} V_S = &\sum_i V_{E_i} + \sum_j V_{I_j} + \sum_{m,n} \kappa_{E_mI_n} V_{E_m} V_{I_n} \\ &+ \sum_{u,w} \kappa_{E_uE_w} V_{E_u} V_{E_w} + \sum_{r,s} \kappa_{I_rI_s} V_{I_r} V_{I_s}, \end{aligned} \tag{3.17}$$

where V_{E_i} and V_{I_j} are the individual EPSP and IPSP, respectively, $\kappa_{E_mI_n}$, $\kappa_{E_uE_w}$, and $\kappa_{I_rI_s}$ are the coefficients encoding the spatiotemporal information of the synaptic inputs with

$$\kappa_{E_uE_w} = \frac{v_{11}(\boldsymbol{x_S}, t; \boldsymbol{x_{E_u}}, \boldsymbol{x_{E_w}}, t_{E_u}, t_{E_w})}{v_{10}(\boldsymbol{x_S}, t; \boldsymbol{x_{E_u}}, t_{E_u}) \cdot v_{10}(\boldsymbol{x_S}, t; \boldsymbol{x_{E_w}}, t_{E_w})} + \mathcal{O}(f_E),$$

$$\kappa_{I_rI_s} = \frac{v_{11}(\boldsymbol{x_S}, t; \boldsymbol{x_{I_r}}, \boldsymbol{x_{I_s}}, t_{I_r}, t_{I_s})}{v_{01}(\boldsymbol{x_S}, t; \boldsymbol{x_{I_r}}, t_{I_r}) \cdot v_{01}(\boldsymbol{x_S}, t; \boldsymbol{x_{I_s}}, t_{I_s})} + \mathcal{O}(f_I),$$

the leading order of which are independent of synaptic input strengths. The generalized bilinear integration rules have also been verified in realistic neuron simulations for synaptic inputs distributed on the branched dendritic tree. As an illustration shown in Figure 3.6, we first verify the special case of the bilinear integration rule when a pair of synaptic inputs of the same type are received on the dendritic trunk either simultaneously or with a 20 ms delay time interval. It is noted that, despite the validity of the bilinear integration rule for a pair of E inputs received on the

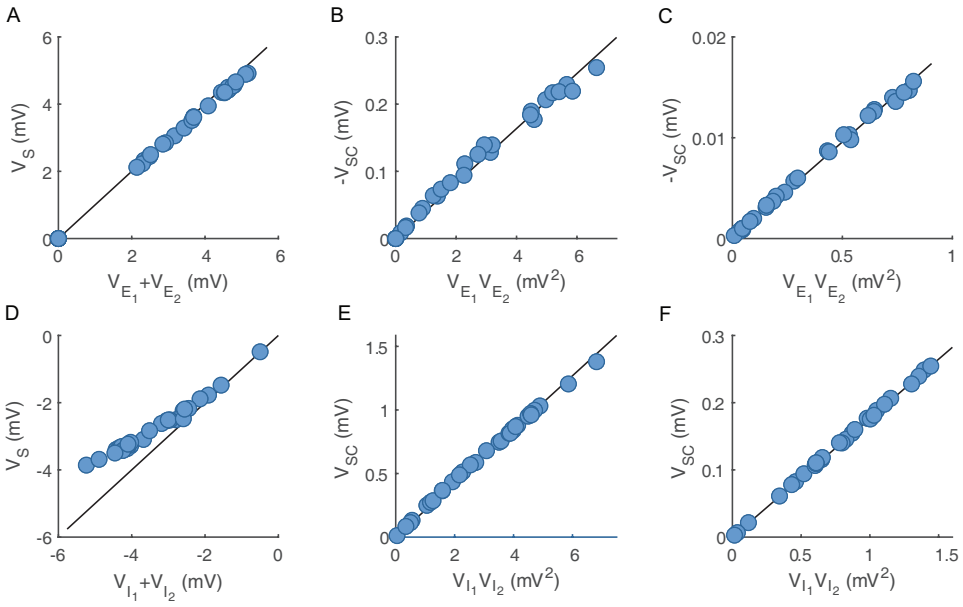

FIGURE 3.6. Integration of two E inputs and two I inputs in the realistic neuron model. (A) The relation between the SC and the linear summation of two EPSPs; (B) the bilinear relation between the SC and the product of the two EPSPs measured at the peak time of one EPSP under the condition when the two EPSPs are induced simultaneously. Each blue dot corresponds to a set of two EPSPs and the corresponding SSP. The black line is linear fitting. The two E inputs are given at the dendritic trunk about 268 μm and 311 μm away from the soma, respectively. (C) The same as (B) except that one EPSP is induced 20 ms later than the other EPSP; (D)–(F) the same as (A)–(C) but for two I inputs.

dendritic trunk, the effect of bilinear integration is small. Accordingly, as shown in Figure 3.6(A), the integration of two E inputs is approximately linear, consistent with experimental observations [10, 11]. The mechanism underlying this phenomenon is that the membrane potential response induced by the E inputs is relatively small compared with the excitatory reversal potential $\varepsilon_E = 70$ mV. Therefore, the driving force $\varepsilon_E - V$ of one synaptic input changes little in the presence of another synaptic input, and the synaptic input current is nearly linearly dependent of the synaptic conductance. This leads to the approximately linear summation of the E inputs. However, in Figure 3.7(A), when an E input is received on a thin dendritic branch, the amplitude of dendritic membrane potential at the input site can be more than ten times larger than the amplitude of somatic membrane potential, and a strong E input can even trigger a dendritic spike. In this case, as shown in Figure 3.7(B), the integration of two E inputs on the same dendritic branch can be substantially sublinear, which is also consistent with previous theoretical and experimental

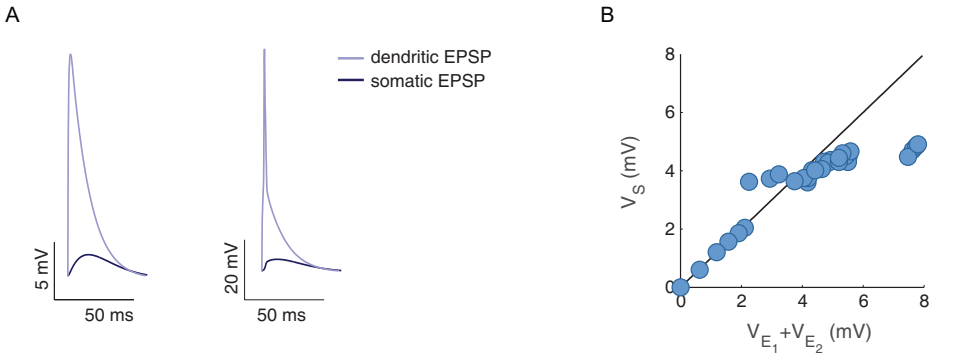

FIGURE 3.7. Integration of two E inputs on the same dendritic branch. (A) Membrane potential change induced by an individual E input measured at the dendritic input site and at the soma. Left and right correspond to the cases of no dendritic spike and dendritic spike, respectively. (B) Relation between the SSP and the linear summation of two EPSPs.

observations [53, 55]. In addition, in Figure 3.7(B) and previous studies [53, 55], the integration of two E inputs can also be superalinear when a dendritic spike is triggered by both of the two E inputs received simultaneously but not by either of them received separately. In these cases, the interaction between two E inputs are too strong such that the bilinear integration rule may no longer hold.

We then verify the general case of the bilinear integration rule when the neuron receives multiple synaptic inputs with stochastic input times and are broadly distributed on the branched dendrites, as shown in Figure 3.8(A),(B). In addition, the membrane potentials measured at three dendritic sites are plotted in Figure 3.8(C)–(E). The result indicates that the integration effect of multiple synaptic inputs can be different across spatial dendrites, which is largely determined by the relative synaptic input locations to the recording sites. The integration effect at a given dendritic site becomes substantial when multiple synaptic inputs are nearby, as shown in Figure 3.8(D).

It can be further analyzed that, different from the spatial asymmetry property of $\kappa_{E_u I_w}$, the spatial dependence of $\kappa_{E_u E_w}$ and $\kappa_{I_r I_s}$ are nearly symmetric. To be specific, for a pair of E inputs, if the location of one input at $\boldsymbol{x}_{\boldsymbol{E_u}}$ is fixed while that of the other input at $\boldsymbol{x}_{\boldsymbol{E_w}}$ varies, the coefficient $\kappa_{E_u E_w}$ reaches its peak value when $\boldsymbol{x}_{\boldsymbol{E_w}}$ overlaps with $\boldsymbol{x}_{\boldsymbol{E_u}}$, and $\kappa_{E_u E_w}$ starts to decay almost in a symmetrical manner as $\boldsymbol{x}_{\boldsymbol{E_w}}$ moves away from $\boldsymbol{x}_{\boldsymbol{E_u}}$ towards both directions—either closer to the soma or further away from the soma. Similarly, $\kappa_{I_r I_s}$ also possesses the property of spatial symmetry as $\kappa_{E_i E_j}$.

4 Reduced Model Incorporating Dendritic Integration

In this section, we investigate the issue of how to incorporate the above dendritic integration rules into a point-neuron model, namely, how to reduce the PDE-based

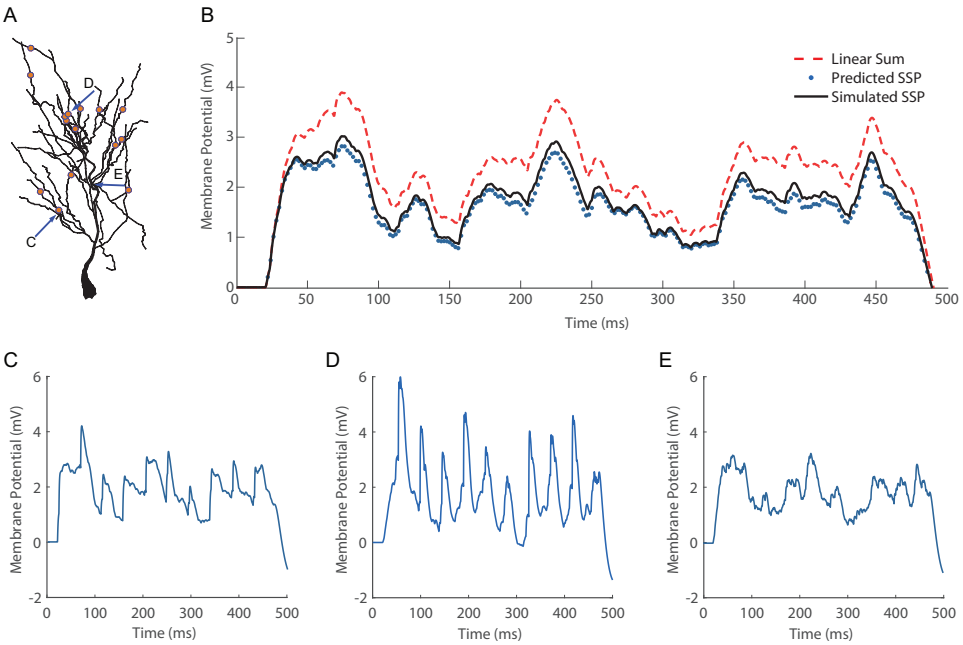

FIGURE 3.8. Integration of multiple E and I synaptic inputs in the realistic neuron model. (A) Distribution of 15 E inputs and 15 I inputs at part of the apical dendrites of the realistic neuron model with length less than 550 μm. The locations of the E and I inputs overlap (orange dots). (B) The traces of the somatic membrane potential obtained by setting the arrival time of each input uniformly distributed from 0 ms to 500 ms. The input rate at each site is 10 Hz. The SSP from the simulation of the realistic neuron model (solid black line) nearly overlaps with the SSP predicted by the bilinear integration rule (equation (3.17)) (blue dots) while deviating from the trace of the linear summation of all postsynaptic potentials induced separately (dashed red line). (C)–(E) Membrane potential response at three different dendritic sites marked by arrows in (A).

cable neuron model (equations (2.6)–(2.10)) to a substantially simpler ODE-based neuron model. The development of such a model is motivated by the fact that the simulation of a neuronal network composed of the branched cable neurons is computationally extremely expensive. This impedes one to study the function of dendrites at the network level to a certain extent. It is thus important to develop a simplified model without the loss of important dendritic functions. The reduced model receiving an individual input is first derived from the cable neuron model, followed by the derivation of the reduced model receiving a pair of E and I synaptic inputs, and finally the reduced model is generalized to the case of multiple E and I synaptic inputs.

4.1 An injecting current input

The traditional way to model a point neuron is based on the idealized assumption that a neuron can be considered as an electrically compact point with its membrane potential dynamics V described by

$$C\frac{dV}{dt} = -G_L V + I_{\text{syn}} + I_{\text{inj}}, \tag{4.1}$$

where C is the capacitance, G_L is the leak conductance, I_{syn} is the synaptic input current, and I_{inj} is the externally injected current.

It has been realized that, because of the highly nonuniform distribution of membrane potential across a neuron with branched dendrites [45, 74], the entire neuron is not electrically compact and thus cannot be simply modeled as a point. On the other hand, by injecting an external current I_{inj} into the soma, it has been shown by experiment that the somatic membrane potential dynamics of a neuron can be well described by a point leaky integrator [3, 8]

$$C\frac{dV}{dt} = -G_L V + I_{\text{inj}}. \tag{4.2}$$

Therefore, equation (4.2) suggests one to model the soma rather than the entire neuron as a point. It is worth mentioning that C and G_L in equation (4.2) are the whole cell property of the neuron measured at the soma. The determination of these parameters will be introduced at the end of Section 4.1.

Despite this experimental observation, there is a lack of theoretical demonstration of how a neuron model with spatial dendritic structure can in general be reduced to the point characterization of its soma (equation (4.2)), and how the parameter sets in the two models relate to each other. In addition, it is unclear how to incorporate synaptic inputs received from the dendrites into the point-neuron model, as the point-neuron model does not explicitly account for dendrites.

The validity of the point-neuron model (equation (4.2)) is first proved below based on the mathematical analysis of the cable neuron model. Again, for the ease of illustration, one can start the analysis with the ball-and-stick neuron model. Given a current impulse input $I_\delta = \delta(x)\delta(t)$ at the soma of the neuron, the ball-and-stick neuron model

$$c\frac{\partial v}{\partial t} = -g_L v + \delta(x)\delta(t) + \frac{d}{4r_a}\frac{\partial^2 v}{\partial x^2}$$

possesses the response kernel (Green's function) evaluated at the soma as $\Gamma(t) = \sum_n H_n e^{-k_n t}$ according to equation (3.15), where constant coefficients H_n and time constants k_n are determined by the geometry and the passive biophysics of the neuron. Asymptotically, the response kernel can be well approximated by its leading order with a single time constant, i.e.,

$$\Gamma(t) \sim H_0 e^{-k_0 t}, \tag{4.3}$$

where $k_0 = g_L/c$,

$$H_0 = [\gamma/(\gamma\lambda + 1)\pi d](4r/c^2 d)^{-1/2} \quad \text{with } \gamma = (\pi d^2/2S)(rd)^{-1/2},$$

and $\lambda = l\sqrt{4r/d}$. Note that equation (4.3) is precisely the response kernel of the point-neuron model (equation (4.2)) with the following relation linking the parameters in the point-neuron model with those in the ball-and-stick neuron model:

$$\begin{aligned} C &= 1/H_0, \\ G_L &= k_0/H_0. \end{aligned} \tag{4.4}$$

For any time-dependent somatic current input, the somatic response of the ball-and-stick neuron can then be described by the convolution of the response kernel (equation (4.3)) of the point-neuron model with the input, thus reducing the somatic membrane potential dynamics of the ball-and-stick neuron with somatic input to its equivalent dynamics of the point neuron (equation (4.2)); equation (4.4) has been further verified numerically with an error below 10%, which demonstrates that the point-neuron characterization is reasonably accurate to represent the somatic membrane potential dynamics of the ball-and-stick neuron. In addition, the validity of the response kernel representation (equation (4.3)) has also been verified numerically in the general case of the cable neuron model with multiple branches.

While it has been shown that the point neuron (equation (4.2)) is an asymptotically valid description of the somatic membrane potential dynamics of a cable neuron with branched dendrites in response to a current injection at the soma, in the remainder of this work the experimentalist's approach is adopted to define the point neuron representation. In practice, it is capable of accurately measuring the leak conductance and membrane capacitance experimentally as follows: by injecting a step current to the soma of the cable neuron model, one can measure the steady-state response V_{steady} when the step current is on and the decay time constant of the voltage response τ_{decay} when the step current is off. According to equation (4.2), $G_L = I_{\text{inj}}/V_{\text{steady}}$ and $C = \tau_{\text{decay}} I_{\text{inj}}/V_{\text{steady}}$.

4.2 An individual synaptic input

In the presence of synaptic current, whether the injected current in equation (4.2) can be simply replaced with the synaptic current remains a question. The question arises from the fact that the synaptic input is in general received on the dendrites spatially away from the soma, which is not explicitly described in the point-neuron model (equation (4.2)). Therefore, to incorporate the synaptic current into the point-neuron model, it first requires a map from the local input on the dendrites to the effective input at the soma. The effective input shall be defined as a hypothetical input received at the soma that induces a response identical to the somatic response induced by the local input received on the dendrites.

The simple case of an individual synaptic input is first considered. Given an individual E input with conductance g_E at location $\boldsymbol{x_E}$ on the dendrites, the cable

neuron model gives

$$c_i \frac{\partial v_i}{\partial t} = -g_{Li} v_i + \frac{d_i}{4r_i} \frac{\partial^2 v_i}{\partial x^2} - g_E(v - \varepsilon_E).$$

The second-order perturbation solution at the soma is solved as

$$V_E = f_E v_{10}(\boldsymbol{x}_S, t) + f_E^2 v_{20}(\boldsymbol{x}_S, t) + \mathcal{O}(f_E^3),$$

where v_{10} and v_{20} are expressed in equations (3.4) and (3.7), respectively. Accordingly, based on the law of current conservation at the soma, the effective synaptic current arriving at the soma from the dendrites can be estimated as

$$\begin{aligned} I_{\text{Esyn}}^{\text{eff}} &= C \frac{dV_E}{dt} + G_L V_E \\ &= f_E \left(C \frac{\partial v_{10}(\boldsymbol{x}_S, t)}{\partial t} + G_L v_{10}(\boldsymbol{x}_S, t) \right) \\ &\quad + f_E^2 \left(C \frac{\partial v_{20}(\boldsymbol{x}_S, t)}{\partial t} + G_L v_{20}(\boldsymbol{x}_S, t) \right) + \mathcal{O}(f_E^3), \end{aligned} \tag{4.5}$$

where C and G_L are the effective capacitance and leak conductance, which can be determined either from the response kernel of the cable neuron model or from experimental measurements as discussed in Section 4.1. We can further define the effective conductance by casting the effective synaptic current (equation (4.5)) in the form of Ohm's law

$$\begin{aligned} G_E^{\text{eff}} &= \frac{I_{\text{Esyn}}^{\text{eff}}}{\varepsilon_E - V_E} \\ &= \frac{1}{\varepsilon_E} \Bigg[f_E \left(C \frac{\partial v_{10}(\boldsymbol{x}_S, t)}{\partial t} + G_L v_{10}(\boldsymbol{x}_S, t) \right) \\ &\quad + f_E^2 \left(C \frac{\partial v_{20}(\boldsymbol{x}_S, t)}{\partial t} + G_L v_{20}(\boldsymbol{x}_S, t) \right) \\ &\quad + f_E^2 \frac{v_{10}(\boldsymbol{x}_S, t)}{\varepsilon_E} \left(C \frac{\partial v_{10}(\boldsymbol{x}_S, t)}{\partial t} + G_L v_{10}(\boldsymbol{x}_S, t) \right) \Bigg] + \mathcal{O}(f_E^3). \end{aligned} \tag{4.6}$$

equation (4.6) together with equations (3.4) and (3.7) establish the map between the local and effective conductance. Therefore, in the presence of an individual E synaptic input, the cable neuron model can be reduced to the point-neuron model to describe the dynamics of its somatic membrane potential

$$C \frac{dV_E}{dt} = -G_L V_E - G_E^{\text{eff}}(V_E - \varepsilon_E), \tag{4.7}$$

with the effective conductance G_E^{eff} defined in equation (4.6).

Similarly, in the presence of an individual I input, the cable neuron model can be reduced to the point-neuron model

$$C \frac{dV_I}{dt} = -G_L V_I - G_I^{\text{eff}}(V_I - \varepsilon_I), \tag{4.8}$$

with the effective conductance G_I^{eff} defined as

$$
\begin{aligned}
G_I^{\text{eff}} = \frac{1}{\varepsilon_I}\Bigg[& f_I\left(C\frac{\partial v_{01}(\boldsymbol{x_S},t)}{\partial t} + G_L v_{01}(\boldsymbol{x_S},t)\right) \\
& + f_I^2\left(C\frac{\partial v_{02}(\boldsymbol{x_S},t)}{\partial t} + G_L v_{02}(\boldsymbol{x_S},t)\right) \\
& + f_I^2\frac{v_{01}(\boldsymbol{x_S},t)}{\varepsilon_I}\left(C\frac{\partial v_{01}(\boldsymbol{x_S},t)}{\partial t} + G_L v_{01}(\boldsymbol{x_S},t)\right)\Bigg] + \mathcal{O}(f_I^3),
\end{aligned} \tag{4.9}
$$

where v_{01} and v_{02} are expressed in equations (3.5) and (3.8).

The accuracy of the second-order approximation to G_E^{eff} and G_I^{eff} has been demonstrated in the simulations of the cable neuron model. In the simulation, an individual E or I input is given on the dendrites of the cable neuron model, and the membrane potential change at the soma V_E or V_I is recorded. Subsequently, the effective synaptic current arriving at the soma is calculated as

$$
I_{\text{Esyn}}^{\text{eff}} = C\frac{dV_E}{dt} + G_L V_E \quad \text{and} \quad I_{\text{Isyn}}^{\text{eff}} = C\frac{dV_I}{dt} + G_L V_I,
$$

and the effective E or I conductance is calculated by its definition

$$
G_E^{\text{eff}} = \frac{I_{\text{Esyn}}^{\text{eff}}}{\varepsilon_E - V_E} \quad \text{and} \quad G_I^{\text{eff}} = \frac{I_{\text{Isyn}}^{\text{eff}}}{\varepsilon_I - V_I}.
$$

As shown in Figure 4.1(A) and 4.1(D), the effective conductance can be well approximated by that obtained from the second-order perturbation solutions in equation (4.6) and equation (4.9).

The effective conductance is a new concept proposed by our perturbation analysis. Although the time scale of the effective and local conductances differs as shown in Figure 4.1(A) and 4.1(D), the effective conductance can be viewed as a proportional indicator of the local conductance on the dendrite as shown in Figure 4.1(B),(C) and 4.1(E),(F). Moreover, it reflects the functional impact of synaptic inputs on the spike initiation mechanism and thereby neuronal information processing at the soma. To be specific, the spike initiation of a neuron is largely determined by the amplitude and the time scale of membrane potential response measured at the soma, and the somatic response depends not only on the local conductance dynamics but also on the synaptic input location [60]. Therefore, knowing the local conductance alone is insufficient to understand how signals are propagated and action potentials are initiated. However, they can be understood from the dynamics of effective conductance that directly determines the somatic membrane potential response. Therefore, measuring the effective conductance can be more valuable than measuring the local conductance for understanding the influence of synaptic activities on somatic membrane potential change and information coding.

4.3 A pair of *E* and *I* synaptic inputs

When a neuron receives more than one synaptic input from the dendrites, it is generally assumed that these synaptic inputs shall be linearly summed when

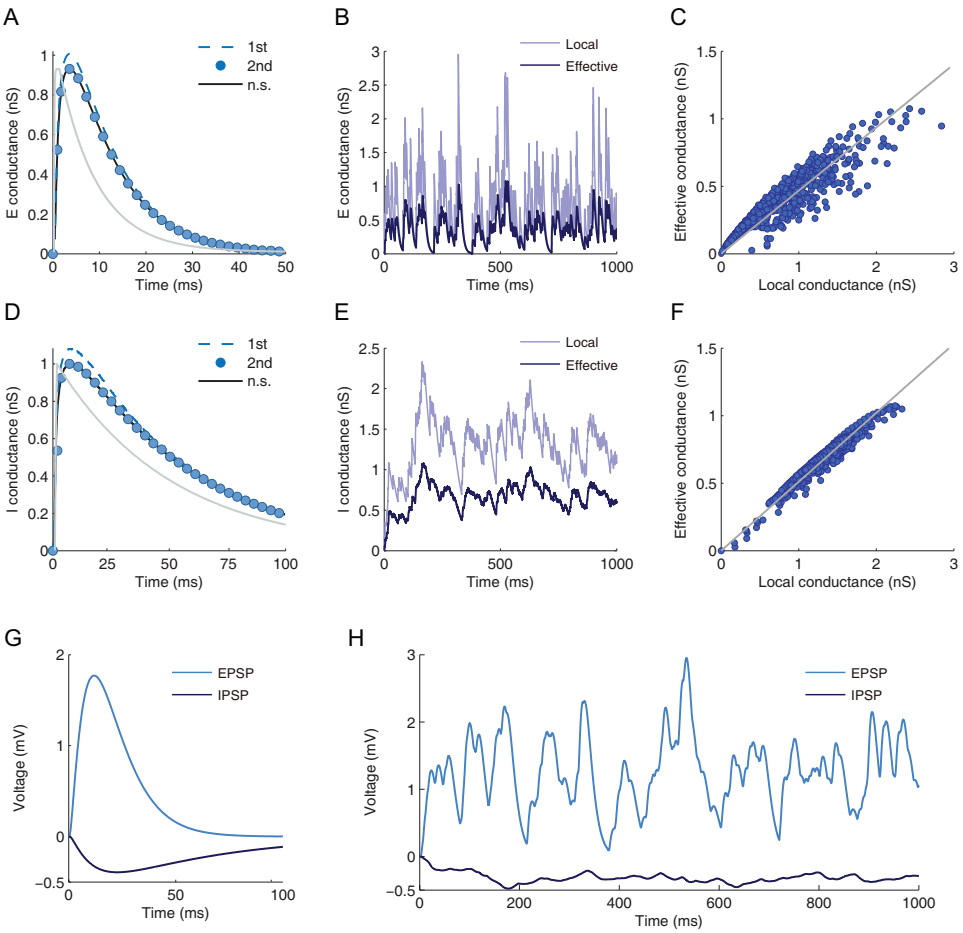

FIGURE 4.1. Properties of the effective synaptic conductance. (A) First-order (dashed blue line) and second-order (blue dots) analytical solutions to approximate the effective E conductance measured in the cable neuron model (solid black line). The normalized local conductance is also plotted in gray. An E input is given on the dendritic trunk 350 μm away from the soma. (B) Trace of the effective and local E synaptic conductances measured respectively at the soma and at a synapse on the dendrite of the cable neuron. Poisson input with rate 150 Hz is given on the dendritic trunk 350 μm away from the soma. (C) Strong correlation between the amplitude of the effective and local E synaptic conductance. Each blue dot is sampled at one time point from the corresponding time series in (B). The gray line is the linear fitting. (D)–(F) The same as (A)–(C) except for the effective and local I synaptic conductance. (G) The corresponding somatic membrane potential responses for (A) and (D). (H) The corresponding somatic membrane potential responses for (B) and (E).

arriving at the soma. Therefore, when a neuron receives a pair of E and I synaptic inputs, the traditional point-neuron model gives

$$C\frac{dV_S}{dt} = -G_L V_S - G_E^{\text{eff}}(V_S - \varepsilon_E) - G_I^{\text{eff}}(V_S - \varepsilon_I). \tag{4.10}$$

As the dendritic integration of synaptic inputs is nonlinear as discussed in Section 3, whether such a model is able to quantitatively capture dendritic integration is questionable. We next investigate the validity of this model using mathematical analysis.

When the neuron receives a pair of E and I synaptic inputs, the SSP measured in the cable neuron model is

$$\begin{aligned} V_S = {} & f_E v_{10}(\boldsymbol{x_S}, t) + f_E^2 v_{20}(\boldsymbol{x_S}, t) + f_I v_{01}(\boldsymbol{x_S}, t) + f_I^2 v_{02}(\boldsymbol{x_S}, t) \\ & + f_E f_I v_{11}(\boldsymbol{x_S}, t) + \mathcal{O}(f^3). \end{aligned}$$

Here $\mathcal{O}(f^3)$ includes all the terms of $\mathcal{O}(f_E^i f_I^j)$ for all $i \geq 0$, $j \geq 0$, and $i + j \geq 3$. Accordingly, the effective synaptic current arriving at the soma is

$$\begin{aligned} I_{\text{Ssyn}}^{\text{eff}} &= C\frac{dV_S}{dt} + G_L V_S \\ &= f_E\Big(C\frac{\partial v_{10}(\boldsymbol{x_S}, t)}{\partial t} + G_L v_{10}(\boldsymbol{x_S}, t)\Big) \\ &\quad + f_E^2\Big(C\frac{\partial v_{20}(\boldsymbol{x_S}, t)}{\partial t} + G_L v_{20}(\boldsymbol{x_S}, t)\Big) \\ &\quad + f_I\Big(C\frac{\partial v_{01}(\boldsymbol{x_S}, t)}{\partial t} + G_L v_{01}(\boldsymbol{x_S}, t)\Big) \\ &\quad + f_I^2\Big(C\frac{\partial v_{02}(\boldsymbol{x_S}, t)}{\partial t} + G_L v_{02}(\boldsymbol{x_S}, t)\Big) \\ &\quad + f_E f_I\Big(C\frac{\partial v_{11}(\boldsymbol{x_S}, t)}{\partial t} + G_L v_{11}(\boldsymbol{x_S}, t)\Big) + \mathcal{O}(f^3) \\ &= I_{\text{Esyn}}^{\text{eff}} + I_{\text{Isyn}}^{\text{eff}} + \Delta I_{\text{syn}}^{\text{eff}}, \end{aligned}$$

where $\Delta I_{\text{syn}}^{\text{eff}}$ is defined as

$$\Delta I_{\text{syn}}^{\text{eff}} = f_E f_I\left(C\frac{\partial v_{11}(\boldsymbol{x_S}, t)}{\partial t} + G_L v_{11}(\boldsymbol{x_S}, t)\right) + \mathcal{O}(f^3). \tag{4.11}$$

From equation (4.11), the leading order of $\Delta I_{\text{syn}}^{\text{eff}}$ is proportional to the product of the input strengths f_E and f_I. Therefore, this current is induced by the nonlinear integration of E and I synaptic currents, thus referred to as the integration current. If the integration current is further cast into the form of Ohm's law, i.e.,

$$\Delta I_{\text{syn}}^{\text{eff}} = -\Delta G_{EI}(V - \varepsilon_{EI}), \tag{4.12}$$

then the integration conductance takes a bilinear form as

$$\Delta G_{EI} = \alpha_{EI} G_E^{\text{eff}} G_I^{\text{eff}}, \tag{4.13}$$

and

$$\alpha_{EI} = \frac{C\big(\varepsilon_E\varepsilon_I\,\partial_t v_{11}(\boldsymbol{x_S},t)+\varepsilon_I\,\partial_t v_{10}(\boldsymbol{x_S},t)v_{01}(\boldsymbol{x_S},t)+\varepsilon_E\,\partial_t v_{01}(\boldsymbol{x_S},t)v_{10}(\boldsymbol{x_S},t)\big)}{\varepsilon_{EI}\big(C\,\partial_t v_{10}(\boldsymbol{x_S},t)+G_L v_{10}(\boldsymbol{x_S},t)\big)\big(C\,\partial_t v_{01}(\boldsymbol{x_S},t)+G_L v_{01}(\boldsymbol{x_S},t)\big)} + \frac{G_L\big(\varepsilon_E\varepsilon_I v_{11}(\boldsymbol{x_S},t)+(\varepsilon_E+\varepsilon_I)v_{10}(\boldsymbol{x_S},t)v_{01}(\boldsymbol{x_S},t)\big)}{\varepsilon_{EI}\big(C\,\partial_t v_{10}(\boldsymbol{x_S},t)+G_L v_{10}(\boldsymbol{x_S},t)\big)\big(C\,\partial_t v_{01}(\boldsymbol{x_S},t)+G_L v_{01}(\boldsymbol{x_S},t)\big)} + \mathcal{O}(f),$$

the leading order of which is independent of the synaptic input strength but is dependent on the input arrival times and locations according to equations (3.4), (3.5), and (3.10). Because of the existence of the integration current, the traditional point-neuron model shall be modified as

$$C\frac{dV_S}{dt} = -G_L V_S - G_E^{\text{eff}}(V_S-\varepsilon_E) - G_I^{\text{eff}}(V_S-\varepsilon_I) - \alpha_{EI}G_E^{\text{eff}}G_I^{\text{eff}}(V_S-\varepsilon_{EI}), \tag{4.14}$$

which is referred to as the DIF model. Note that, according to our analysis, there is a degree of freedom for choosing the value of the reversal potential ε_{EI} within the regime in which the ratio of the postsynaptic potential to the reversal potential is small, and the value of the integration coefficient α_{EI} depends on the choice of the reversal potential. However, the bilinear interaction between the conductances remains valid when choosing a different reversal potential value.

Based on our analysis, the integration current and the DIF model (equation (4.14)) are in general valid for a pair of E and I synaptic inputs distributed on any dendritic branches with arbitrary arrival times. Next, realistic neuron simulation is performed to confirm the form of the integration current (equations (4.12)–(4.13)) and further the validity of the point-neuron model. In the simulation, an EPSP or an IPSP is measured at the soma denoted as V_E or V_I after giving an individual E synaptic input on the dendrite about 311 μm away from the soma or an individual I synaptic input on the dendrite about 268 μm away from the soma, respectively. The effective E and I synaptic currents

$$I_{\text{Esyn}}^{\text{eff}} = C\frac{dV_E}{dt} + G_L V_E \quad \text{and} \quad I_{\text{Isyn}}^{\text{eff}} = C\frac{dV_I}{dt} + G_L V_I$$

and the effective conductances at the soma

$$G_E^{\text{eff}} = \frac{I_{\text{Esyn}}^{\text{eff}}}{\varepsilon_E - V_E} \quad \text{and} \quad G_I^{\text{eff}} = \frac{I_{\text{Isyn}}^{\text{eff}}}{\varepsilon_I - V_I}$$

are determined by V_E and V_I, respectively. The neuron is then stimulated given both the E and I synaptic inputs simultaneously with the input strengths and input locations being identical to those given individually, and an SSP is measured at the soma denoted as V_S and the corresponding summed somatic current (SSC) is calculated as

$$I_{\text{Ssyn}}^{\text{eff}} = C\frac{dV_S}{dt} + G_L V_S.$$

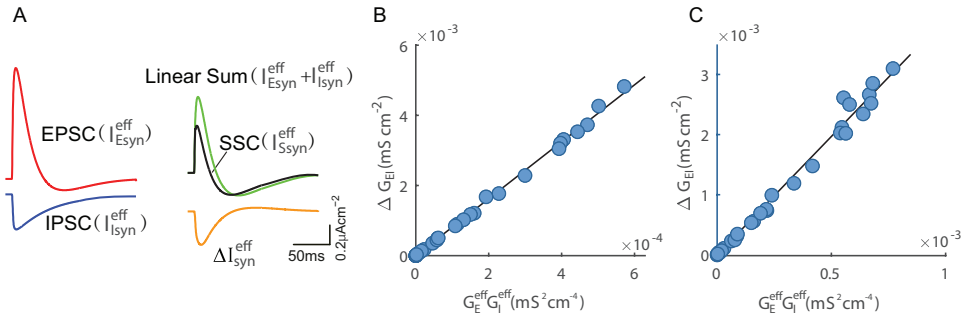

FIGURE 4.2. Integration of effective E and I conductances in the realistic neuron model. (A) A set of EPSC (red line), IPSC (blue line), and SSC (black line) measured in the realistic neuron model. The linear sum (green line) and the integration current (orange line) are calculated correspondingly. (B) The bilinear relation between the integration conductance ΔG_{EI} and the product of the effective E and I conductances G_E^{eff} and G_I^{eff} at the peak time of G_E^{eff} when the EPSP and the IPSP are induced simultaneously. Each blue dot corresponds to a set of G_E^{eff}, G_I^{eff}, and ΔG_{EI}. The black line is linear fitting. The E and I inputs are given on the dendritic trunk about 311 μm and 268 μm away from the soma, respectively. (C) The same as (B) except that the EPSP is induced 20 ms later than the IPSP.

After constructing the excitatory postsynaptic current (EPSC) and the inhibitory postsynaptic current (IPSC) as $G_E^{\text{eff}}(\varepsilon_E - V_S)$ and $G_I^{\text{eff}}(\varepsilon_I - V_S)$ respectively, the SSC is found to be significantly different from the linear summation of the constructed EPSC and IPSC, as shown in Figure 4.2(A). This indicates the existence of the synaptic integration current predicted from the perturbation analysis.

The difference between the SSC and the linear summation of the constructed EPSC and IPSC is denoted as

$$\Delta I_{\text{syn}}^{\text{eff}} = I_{\text{Ssyn}}^{\text{eff}} - I_{\text{Esyn}}^{\text{eff}} - I_{\text{Isyn}}^{\text{eff}}.$$

Further, the integration conductance ΔG_{EI} obtained from $\Delta I_{\text{syn}}^{\text{eff}}$ is calculated as

$$\Delta G_{EI} = \frac{I_{\text{syn}}^{\text{eff}}}{\varepsilon_{EI} - V_S}.$$

By randomly varying the strengths of the E and I inputs with their input locations fixed, the integration conductance ΔG_{EI} is indeed shown to be proportional to both G_E^{eff} and G_I^{eff} at each time point, confirming the bilinear relation

$$\Delta G_{EI} = \alpha_{EI} G_E^{\text{eff}} G_I^{\text{eff}}.$$

The bilinear relation at a particular time point around the peak of the EPSP is illustrated in Figure 4.2(B). The bilinear relation remains valid even when the E and I inputs do not arrive simultaneously. As an illustration, a particular case of

the bilinear relation is shown in Figure 4.2(C) when the I input is elicited 20 ms earlier than the E input. Consistent with our theoretical predictions, the integration coefficient α_{EI} in the bilinear relation is found to be independent of input strengths but is dependent on input arrival times.

4.4 Spatiotemporal dependence of α_{EI}

The spatiotemporal dependence of α_{EI} can be obtained from that of κ_{EI} discussed in Section 3.2 through a one-to-one mathematical map from α_{EI} to κ_{EI} derived below. Based on the DIF model, the individual EPSP denoted by V_E and IPSP denoted by V_I under separate E and I inputs shall be described by equation (4.7) and equation (4.8), respectively, whereas the SSP denoted by V_S under joint E and I inputs shall be described by equation (4.14). With notations

$$\begin{aligned} G_S^{\text{eff}} &= G_E^{\text{eff}} + G_I^{\text{eff}} + \alpha_{EI} G_E^{\text{eff}} G_I^{\text{eff}}, \\ I_S^{\text{rev}} &= \varepsilon_E G_E^{\text{eff}} + \varepsilon_I G_I^{\text{eff}} + \alpha_{EI} \varepsilon_{EI} G_E^{\text{eff}} G_I^{\text{eff}}, \end{aligned}$$

one can obtain analytical solutions to equations (4.7), (4.8), (4.14) along with their approximations in an integral form as

$$\begin{aligned} V_E(t) &= \int_0^t \frac{\varepsilon_E G_E^{\text{eff}}(u)}{C} e^{G_L(u-t)/C} e^{\int_t^u G_E^{\text{eff}}(v)/C\,dv} du \\ &= \int_0^t \frac{\varepsilon_E G_E^{\text{eff}}(u)}{C} e^{G_L(u-t)/C} \left(1 + \int_t^u G_E^{\text{eff}}(v)/C dv\right) du \\ &\quad + \mathcal{O}(f_E^3), \end{aligned} \tag{4.15}$$

$$\begin{aligned} V_I(t) &= \int_0^t \varepsilon_I \frac{G_I^{\text{eff}}(u)}{C} e^{G_L(u-t)/C} e^{\int_t^u G_I^{\text{eff}}(v)/C\,dv} du \\ &= \int_0^t \varepsilon_I \frac{G_I^{\text{eff}}(u)}{C} e^{G_L(u-t)/C} \left(1 + \int_t^u G_I^{\text{eff}}(v)/C dv\right) du \\ &\quad + \mathcal{O}(f_I^3), \end{aligned} \tag{4.16}$$

$$\begin{aligned} V_S(t) &= \int_0^t \frac{I_S^{\text{rev}}}{C} e^{G_L(u-t)/C} e^{\int_t^u G_S^{\text{eff}}(v)/C\,dv} du \\ &= \int_0^t \frac{I_S^{\text{rev}}}{C} e^{G_L(u-t)/C} \left(1 + \int_t^u G_S^{\text{eff}}(v)/C dv\right) du + \mathcal{O}(f^3), \end{aligned} \tag{4.17}$$

where the approximations are taken with respect to the second order of $\int_t^u G_E^{\text{eff}}(s)ds$, $\int_t^u G_I^{\text{eff}}(s)ds$, and $\int_t^u G_S^{\text{eff}}(s)ds$ in Taylor expansion. All the above approximations have been numerically verified that the relative error between the analytical and approximate solutions was less than 5%.

Then by the definition of the shunting coefficient κ_{EI}, together with equations (4.15)–(4.17), one has

$$\kappa_{EI} \equiv \frac{V_S - V_E - V_I}{V_E \cdot V_I} = A\alpha_{EI} + B + \mathcal{O}(f), \tag{4.18}$$

where A and B are defined as

$$A = \frac{\varepsilon_{EI} C \int_0^t G_E^{\text{eff}}(u) G_I^{\text{eff}}(u) e^{G_L(u-t)/C}\, du}{\varepsilon_E \varepsilon_I Q(G_I^{\text{eff}}, t) Q(G_E^{\text{eff}}, t)},$$

$$B = -\frac{\int_0^t \left[\varepsilon_E G_I^{\text{eff}}(u) Q(G_E^{\text{eff}}, u) + \varepsilon_I G_E^{\text{eff}}(u) Q(G_I^{\text{eff}}, u)\right] du}{\varepsilon_E \varepsilon_I Q(G_E^{\text{eff}}, t) Q(G_I^{\text{eff}}, t)},$$

and $Q(f, x)$ is defined as $Q(f, x) = \int_0^x e^{G_L(y-t)/C} f(y) dy$. equation (4.18) establishes a one-to-one map from α_{EI} to κ_{EI}. Because A and B are independent of input strengths as they cancel out in both the denominator and the numerator, and α_{EI} is also independent of input strengths, thus the leading order of κ_{EI} is a constant independent of input strengths. Therefore, the DIF model (equation (4.14)) is proved to be able to capture the bilinear integration rule discovered in Section 3.1. In addition, from the map (equation (4.18)), similarly to κ_{EI}, α_{EI} is also spatiotemporally dependent and possesses the feature of spatial asymmetry.

4.5 Multiple synaptic inputs

When a neuron receives multiple E and I inputs, the membrane potential dynamics can be naturally generalized as

$$C\frac{dV_S}{dt} = -G_L V_S - \sum_i G_{Ei}^{\text{eff}}(V_S - \varepsilon_E) - \sum_j G_{Ij}^{\text{eff}}(V_S - \varepsilon_I) + \Delta I_{\text{syn}}^{\text{eff}}, \tag{4.19}$$

where the synaptic integration current $\Delta I_{\text{syn}}^{\text{eff}}$ is described as

$$\begin{aligned} \Delta I_{\text{syn}}^{\text{eff}} = &\sum_m \sum_n \alpha_{EI}^{mn} G_{Em}^{\text{eff}} G_{In}^{\text{eff}} (\varepsilon_{EI} - V_S) \\ &+ \sum_p \sum_q \alpha_{EE}^{pq} G_{Ep}^{\text{eff}} G_{Eq}^{\text{eff}} (\varepsilon_E - V_S) \\ &+ \sum_s \sum_t \alpha_{II}^{st} G_{Is}^{\text{eff}} G_{It}^{\text{eff}} (\varepsilon_I - V_S). \end{aligned} \tag{4.20}$$

The synaptic integration current describes the interaction of each pair of synaptic inputs, and the sets of integration coefficients $\{\alpha_{EI}^{mn}\}$, $\{\alpha_{EE}^{pq}\}$, and $\{\alpha_{II}^{st}\}$ encode the spatiotemporal information of synaptic inputs on the dendrites. In addition to the synaptic current description (equation (4.19)), by incorporating the synaptic integration current (equation (4.20)), the DIF model accurately characterizes the synaptic currents arriving at the soma.

As demonstrated from our realistic neuron simulations shown in Figure 4.3(A) and 4.3(D), for the special case when the realistic neuron model receives a pair of

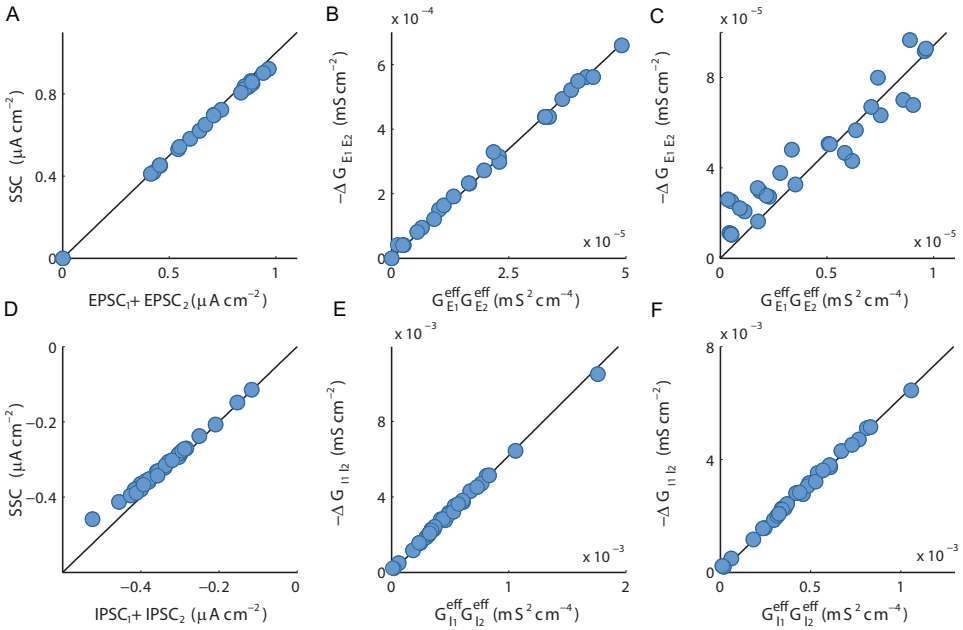

FIGURE 4.3. Integration of effective *E*-*E* and *I*-*I* conductances in the realistic neuron model. (A) The relation between the SSC induced by two simultaneous *E* inputs and the linear sum of the two EPSCs induced by two separate *E* inputs. Data are measured at the peak time of $G_{E_1}^{\text{eff}}$. Each blue dot corresponds to a set of SSC, EPSC_1, and EPSC_2. The black line is linear fitting. The two *E* inputs are given on the dendritic trunk about 311 μm and 268 μm away from the soma, respectively. (B) The bilinear relation between the integration conductance $\Delta G_{E_1E_2}$ and the product of the two effective *E* conductances $G_{E_1}^{\text{eff}}$ and $G_{E_2}^{\text{eff}}$ when the two *E* inputs are received simultaneously. The input information is the same as in (A). (C) The same as (B) except that one *E* input is received 10 ms later than the other *E* input. (D)–(F) The same as (A)–(C) except for the *I* input case.

E inputs or a pair of *I* inputs on the dendrites, the SSC is different from the linear summation of the two EPSCs or the two IPSCs induced individually. It has been observed that the integration between the two EPSCs is more linear than that between the two IPSCs. This observation is consistent with the integration between two EPSPs and IPSPs as shown in Figure 3.6(A) and 3.6(D), as it also attributes to the substantial difference between the *E* and *I* reversal potentials. Despite this, the bilinear form of the integration conductance remains valid for both the *E*-*E* case and the *I*-*I* case, as shown in Figure 4.3. For the integration of multiple synaptic inputs, given tens of or even hundreds of E and I synaptic inputs from its dendrites with uniformly distributed arrival times, the somatic membrane potential of the realistic neuron model nearly overlaps with the SSP predicted by the DIF model with

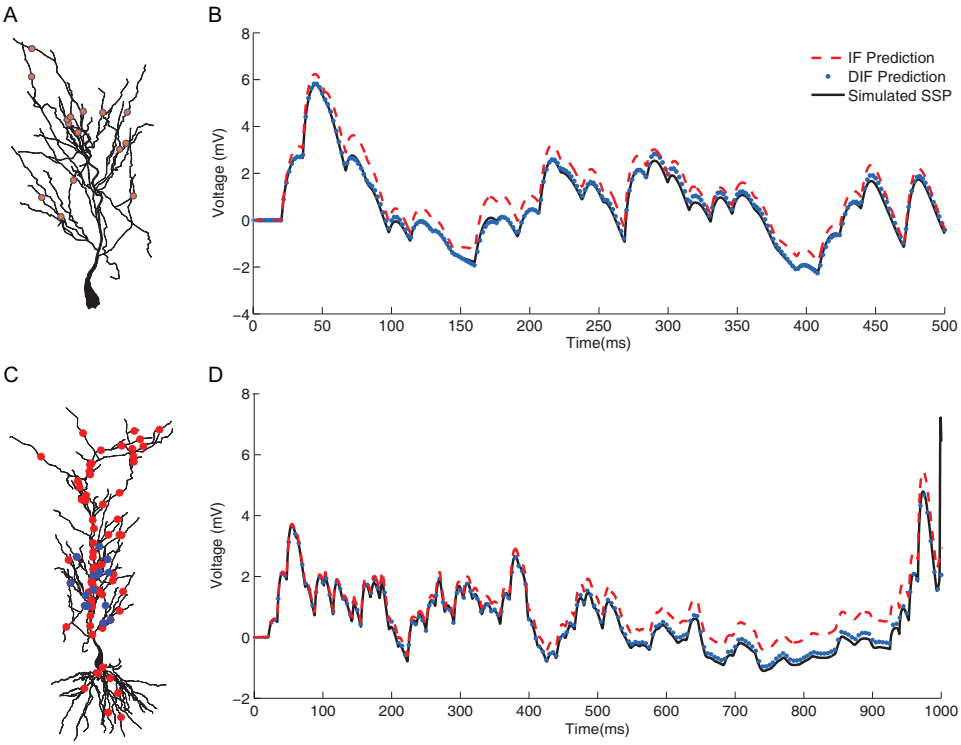

FIGURE 4.4. Integration of multiple E and I inputs in the realistic neuron model. (A) Distribution of 15 E inputs and 15 I inputs at part of the apical dendrites of the realistic neuron model with length less than 550 μm. The locations of the E and I inputs overlap (orange dots). (B) One trial of membrane potential obtained by setting the arrival time of each stimulus uniformly distributed from 0 ms to 500 ms. The SSP from the simulation of the realistic neuron model (solid black line) nearly overlaps with the SSP predicted by the DIF model (blue dots) while deviating from the trace of the IF model without including the integration current (dashed red line). (C) Distribution of 75 E inputs (red dots) and 25 I inputs (blue dots) at the whole dendrites of the realistic neuron model. (D) One trial of membrane potential obtained by setting the arrival time of each stimulus uniformly distributed from 0 ms to 1000 ms. Panel (B) and panel (D) share the same figure legend.

the synaptic integration current (equations (4.19)–(4.20)) while deviating from the SSP predicted by the point-neuron model without the synaptic integration current, as shown in Figure 4.4.

The DIF model (equations (4.19)–(4.20)) provides an efficient computational framework for simulation of large-scale neuronal networks. The performance of the DIF model is evaluated by contrasting its computational cost to that of the cable neuron model. When simulating a morphologically realistic pyramidal neuron,

it generally requires one to discretize the space of the cable PDEs into approximately $N_1 = 10^5$ spatial points (for example, the dendrites consist of about 200 to 300 segments, each segment being further discretized as about a hundred compartments described by ODEs) at which the temporal dynamics of membrane potentials is computed. The computational cost to solve these ODEs is $\mathcal{O}(N_1)$ (e.g., using the forward Euler scheme). In addition, based on the fact that a cortical pyramidal neuron in vivo receives about $N_2 = 10^4$ synaptic inputs [15], there are additional $\mathcal{O}(N_2)$ ODEs to describe the temporal evolution of synaptic conductances. Therefore, the computational complexity is $\mathcal{O}(N_1) + \mathcal{O}(N_2)$ for evolving an individual time step of the membrane potential on all the dendrites of a single neuron. When simulating a network of N neurons, the computational complexity scales up to $N(\mathcal{O}(N_1) + \mathcal{O}(N_2))$. In contrast, simulating the DIF model only requires one to numerically solve $\mathcal{O}(N_2)$ for one time step evolution of the membrane potential and synaptic conductances. However, additional cost shall be considered due to the bilinear integration of synaptic inputs. As cortical pyramidal neurons typically fire about 10 spikes per second in awake animals [77, 78], a pyramidal neuron can be expected to receive 10^5 synaptic inputs per second. Therefore, the average number of synaptic inputs within 10 ms (the scale of the membrane potential time constant in vivo) is 10^3. In principle, there are 10^6 bilinear interactions for all pairs of inputs. However, it has been shown that the majority of these interactions are small as the nonlinear interaction is mainly localized within a branch. Correspondingly, the number of bilinear interactions linearly scales with synaptic input numbers [39], which is about $N_3 = 10^3$. Therefore, the computational complexity for the bilinear interaction is $\mathcal{O}(N_3)$ for the evolution of each time step, and the computational complexity is $\mathcal{O}(N_2) + \mathcal{O}(N_3)$ for evolving an individual time step of the membrane potential of each DIF neuron. When simulating a network of N neurons, the computational complexity scales up to $N(\mathcal{O}(N_2) + \mathcal{O}(N_3))$. Therefore, the DIF model outperforms the cable neuron model by reducing a computational cost of $N(\mathcal{O}(N_1) - \mathcal{O}(N_3))$. In practice, the reduced computational cost can be higher because a smaller time step is often required to meet the stability condition when solving the cable neuron model. Furthermore, it should be noted that the bilinear integration of synaptic conductances can be computed in parallel with an easy implementation, which will further save computation time.

In the above computational framework, one is required to look up a library established in advance to store the integration coefficients for the interaction between each pair of inputs. In the case of passive dendrites, the integration coefficients in the library can be calculated analytically based on equation (4.13). However, in practice, it is more convenient for one to calculate the integration coefficients by directly simulating the realistic neuron model and measuring the synaptic conductance when the realistic neuron model receives a pair of synaptic inputs separately and then together. The library of integration coefficients shall take the form of a set of matrices (or a high-dimensional tensor): the row and column indices of each

matrix correspond to synaptic input locations, and the elements in each matrix correspond to the integration coefficient measured at a particular time point t when a pair of inputs are received with a particular arrival time difference τ. Different matrices are labeled by the time t and the arrival time interval τ. Note that the establishment of the library can be accomplished in a parallel fashion in order to save computation time. In addition, the establishment of the library only requires one-time computation. Later simulations of the same neuron model can directly use the established library with no need to re-establish a new one.

5 Discussion

In this work, we provide a systematic theoretical analysis of the branched cable neuron model to investigate the dendritic integration of biological neurons. The branched cable neuron model has been introduced to describe the subthreshold membrane potential dynamics of a biological neuron, and the second-order perturbation solutions have been derived and verified to well approximate the response at the soma of the neuron when receiving conductance-based synaptic inputs. By using the perturbation solutions, a bilinear integration rule has been identified that captures the integrated somatic membrane potential in response to multiple spatiotemporal synaptic inputs. In addition, the perturbation solutions further lead to a model reduction from the PDE-based spatial cable neuron model to the ODE-based effective point-neuron model with the bilinear integration rule inherited, which provides an efficient computational framework of neuronal simulation incorporating certain important dendritic functions. All the theoretical results have been further extended by numerical verification of the realistic neuron model with biologically plausible morphological and biophysical properties.

In our modeling and analysis, we consider the realistic case that a neuron receives synaptic input current that depends on both the synaptic conductance and the voltage, in contrast to other analytical works that often treat synaptic input current as voltage-independent current. Accordingly, the model neuron possesses the feature of a nonlinear device, i.e., the membrane potential change in response to a synaptic input depends nonlinearly on the synaptic conductance, even when the membrane potential stays in the subthreshold regime before generating action potentials. The mathematical origin of the nonlinear input-output relation of a neuron lies in the form of the synaptic input current $I_{\text{syn}} = g_{\text{syn}}(\varepsilon_{\text{syn}} - V)$, in which I_{syn} depends not only on the synaptic conductance g_{syn} but also on the membrane potential (voltage) V explicitly. Such a feedback mechanism (I_{syn} changes V, and V also affects I_{syn}) breaks down the principle of linear superposition in the voltage dynamics of the neuron, giving rise to the phenomenon of nonlinear dendritic integration when the neuron receives multiple synaptic inputs, as demonstrated in our work.

To capture the nonlinear input-output relation, we solve the cable neuron model (equations (2.6)–(2.10)) using a regular perturbation method. By taking the fact that strengths of synaptic inputs are small, the membrane potential response can be

represented as a series in the powers of synaptic strengths (equation (3.1)). Consequently, we can obtain a hierarchy of linear cable equations with explicitly known current inputs, and analytically derive the corresponding perturbation solutions to all orders (equations (3.3)–(3.10)). A detailed calculation for the case of a pair of E and I inputs is shown in Section 3.1. Without providing a rigorous error analysis, we instead have verified the accuracy of the perturbation solutions to various orders by comparing them with the numerical solutions of the cable model. Numerical results show that second-order perturbation solutions are reasonably accurate in capturing the neuronal membrane potential change in response to synaptic inputs for input strengths in realistic physiological regimes.

The perturbation scheme works well to reveal the nonlinear dendritic integration effect in the passive neuron model because it captures the mechanism underlying nonlinear interaction among synaptic inputs, i.e., that the driving force of one synaptic input is changed by another synaptic input from a different dendritic location. In addition, as the change of membrane potential at one synapse by another synaptic input is relatively small in general, second-order truncation of the perturbation series is sufficient to capture the nonlinear dendritic integration effect, leading to the bilinear dendritic integration rule. In the nonlinear case of active dendrites, there is no Green's function; thus the direct verification of the second-order perturbation scheme is challenging. However, in certain active dendrite cases, the bilinear integration rule derived from the perturbation scheme in the passive dendrite case can still be verified numerically, indicating the validity of the perturbation scheme beyond the case of passive dendrites. The bilinear rule breaks down when the interaction between the synaptic inputs is too strong to be captured by the second-order perturbation scheme, e.g., when a dendritic spike is generated near the I input location as shown in Figure 3.3(C). Therefore, a practical way to validate the perturbation method is either to check the level of dendritic activities, or alternatively to check the validity of the bilinear integration rule that requires the second-order perturbation solutions to hold.

It is expected that our theoretical and computational framework can be extended to study many other important scientific questions related to dendritic functions. For instance, using the same framework presented in this paper, we have identified the severe drawback of conductance measurement using traditional clamping methods. In addition, we have developed methods to recover both the effective and local synaptic conductances under somatic voltage clamp or current clamp. By overcoming the challenge of the space clamp effect, the recovery of the synaptic conductance from voltage measurements is an important step toward understanding neuronal dendritic computation. This work will be published elsewhere.

Despite the successful analysis to understand dendritic integration, there remain some questions for future investigations. First, the bilinear dendritic integration rule identified in our work demonstrates that the interaction of multiple inputs can be decomposed into the summation of pairwise interactions for all pairs of synaptic

inputs. Numerical simulation shows that this rule may break down when the realistic neuron receives hundreds of synaptic inputs *in a short time window*. In such a case, the bilinear integration must be modified by taking into account higher-order interactions. Second, as the perturbation analysis is performed in the passive cable model, the derived bilinear integration rule may break down when strong nonlinearity occurs on the dendrites, including dendritic spikes and plateau potentials. The description of active dendritic computation requires the modification of the current form of the dendritic integration rule. Third, the dendritic integration studied in this work is limited to the subthreshold regime without accounting for active channels associated with spike generation. This limitation can possibly be overcome by modeling spike generation through a firing threshold such as integrate-and-fire representations. To fully understand neuronal dendritic integration, all these questions require further investigation, which goes beyond the regular perturbation analysis performed in this work.

Acknowledgment. The authors dedicate this work to Professor David Cai. This work is supported by National Key R&D Program of China 2019YFA0709503; Shanghai Municipal Science and Technology Major Project 2021SHZDZX0102 (S.L., D.Z.); Natural Science Foundation of China Grant 11901388; Shanghai Sailing Program 19YF1421400; Shanghai Chengguang Program (S.L.); Natural Science Foundation of China Grants 12071287, 11671259, 11722107; SJTU-UM Collaborative Research Program (D.Z.); and by the Student Innovation Center at Shanghai Jiao Tong University.

Bibliography

[1] Andrásfalvy, B. K.; Magee, J. C. Distance-dependent increase in AMPA receptor number in the dendrites of adult hippocampal CA1 pyramidal neurons. *The Journal of Neuroscience* **21** (2001), no. 23, 9151–9159. doi:10.1523/JNEUROSCI.21-23-09151.2001

[2] Atallah, B.; Scanziani, M. Instantaneous modulation of gamma oscillation frequency by balancing excitation with inhibition. *Neuron* **62** (2009), no. 4, 566–577. doi:10.1016/j.neuron.2009.04.027

[3] Badel, L.; Lefort, S.; Brette, R.; Petersen, C. C.; Gerstner, W.; Richardson, M. J. Dynamic IV curves are reliable predictors of naturalistic pyramidal-neuron voltage traces. *Journal of Neurophysiology* **99** (2008), no. 2, 656–666. doi:10.1152/jn.01107.2007

[4] Behabadi, B. F.; Polsky, A.; Jadi, M.; Schiller, J.; Mel, B. W. Location-dependent excitatory synaptic interactions in pyramidal neuron dendrites. *PLoS Comput. Biol.* **8** (2012), no. 7, e1002599. doi:10.1371/journal.pcbi.1002599

[5] Bracewell, R. N. *The Fourier transform and its applications.* Third edition. McGraw-Hill Series in Electrical Engineering. Circuits and Systems. McGraw-Hill, New York, 1986.

[6] Branco, T.; Clark, B. A.; Häusser, M. Dendritic discrimination of temporal input sequences in cortical neurons. *Science* **329** (2010), no. 5999, 1671–1675. doi:10.1126/science.1189664

[7] Cannon, R.; Turner, D.; Pyapali, G.; Wheal, H. An on-line archive of reconstructed hippocampal neurons. *Journal of Neuroscience Methods* **84** (1998), no. 1, 49–54. doi:10.1016/S0165-0270(98)00091-0

[8] Carandini, M.; Mechler, F.; Leonard, C. S.; Movshon, J. A. Spike train encoding by regular-spiking cells of the visual cortex. *Journal of Neurophysiology* **76** (1996), no. 5, 3425–3441. doi:10.1152/jn.1996.76.5.3425

[9] Carnevale, N.; Hines, M. *The NEURON book*. Cambridge University Press, Cambridge, 2006.

[10] Cash, S.; Yuste, R. Input summation by cultured pyramidal neurons is linear and position-independent. *Journal of Neuroscience* **18** (1998), no. 1, 10–15. doi:10.1523/JNEUROSCI.18-01-00010.1998

[11] Cash, S.; Yuste, R. Linear summation of excitatory inputs by CA1 pyramidal neurons. *Neuron* **22** (1999), no. 2, 383–394. doi:10.1016/S0896-6273(00)81098-3

[12] Chacron, M. J. Nonlinear information processing in a model sensory system. *Journal of Neurophysiology* **95** (2006), no. 5, 2933–2946. doi:10.1152/jn.01296.2005

[13] David, F.; Linster, C.; Cleland, T. A. Lateral dendritic shunt inhibition can regularize mitral cell spike patterning. *Journal of Computational Neuroscience* **25** (2008), no. 1, 25–38. doi:10.1007/s10827-007-0063-5

[14] Dayan, P.; Abbott, L. *Theoretical neuroscience: Computational and mathematical modeling of neural systems*. MIT Press, Cambridge, Mass., 2001.

[15] DeFelipe, J.; Fariñas, I. The pyramidal neuron of the cerebral cortex: morphological and chemical characteristics of the synaptic inputs. *Progress in Neurobiology* **39** (1992), no. 6, 563–607. doi:10.1016/0301-0082(92)90015-7

[16] Destexhe, A.; Mainen, Z. F.; Sejnowski, T. J. An efficient method for computing synaptic conductances based on a kinetic model of receptor binding. *Neural Computation* **6** (1994), no. 1, 14–18. doi:10.1162/neco.1994.6.1.14

[17] Destexhe, A.; Mainen, Z. F.; Sejnowski, T. J. Synthesis of models for excitable membranes, synaptic transmission and neuromodulation using a common kinetic formalism. *Journal of Computational Neuroscience* **1** (1994), no. 3, 195–230. doi:10.1007/BF00961734

[18] Destexhe, A.; Mainen, Z. F.; Sejnowski, T. J. Kinetic models of synaptic transmission. *Methods in Neuronal Modeling* **2** (1998), 1–25.

[19] FitzHugh, R. Impulses and physiological states in theoretical models of nerve membrane. *Biophysical Journal* **1** (1961), no. 6, 445–466. doi:10.1016/S0006-3495(61)86902-6

[20] Fotowat, H.; Gabbiani, F. Collision detection as a model for sensory-motor integration. *Annual Review of Neuroscience* **34** (2011), 1–19. doi:10.1146/annurev-neuro-061010-113632

[21] Gabbiani, F.; Krapp, H. G.; Koch, C.; Laurent, G. Multiplicative computation in a visual neuron sensitive to looming. *Nature* **420** (2002), no. 6913, 320–324. doi:10.1038/nature01190

[22] Gidon, A.; Segev, I. Principles governing the operation of synaptic inhibition in dendrites. *Neuron* **75** (2012), no. 2, 330–341. doi:10.1016/j.neuron.2012.05.015

[23] Grienberger, C.; Chen, X.; Konnerth, A. NMDA receptor-dependent multidendrite Ca2+ spikes required for hippocampal burst firing in vivo. *Neuron* **81** (2014), no. 6, 1274–1281. doi:10.1016/j.neuron.2014.01.014

[24] Hao, J.; Wang, X.; Dan, Y.; Poo, M.; Zhang, X. An arithmetic rule for spatial summation of excitatory and inhibitory inputs in pyramidal neurons. *Proc. Natl. Acad. Sci. USA* **106** (2009), no. 51, 21906–21911. doi:10.1073/pnas.0912022106

[25] Häusser, M.; Roth, A. Estimating the time course of the excitatory synaptic conductance in neocortical pyramidal cells using a novel voltage jump method. *Journal of Neuroscience* **17** (1997), no. 20, 7606–7625. doi:10.1523/JNEUROSCI.17-20-07606.1997

[26] Hodgkin, A. L.; Huxley, A. F. A quantitative description of membrane current and its application to conduction and excitation in nerve. *The Journal of Physiology* **117** (1952), no. 4, 500–544. doi:10.1113/jphysiol.1952.sp004764

[27] Hoffman, D. A.; Magee, J. C.; Colbert, C. M.; Johnston, D. K^+ channel regulation of signal propagation in dendrites of hippocampal pyramidal neurons. *Nature* **387** (1997), no. 6636, 869–875.

[28] Holmes, W. R. A continuous cable method for determining the transient potential in passive dendritic trees of known geometry. *Biological Cybernetics* **55** (1986), no. 2-3, 115–124. doi:10.1007/BF00341927

[29] Holmes, W. R. *Morphoelectrotonic transform*. Springer, New York, 2013. doi:10.1007/978-1-4614-7320-6_481-1

[30] Izhikevich, E. M. Simple model of spiking neurons. *IEEE Transactions on Neural Networks* **14** (2003), no. 6, 1569–1572. doi:10.1109/TNN.2003.820440

[31] Jack, J. J. B.; Noble, D.; Tsien, R. W. *Electric current flow in excitable cells*. Clarendon Press, Oxford, 1975.

[32] Jadi, M. P.; Behabadi, B. F.; Poleg-Polsky, A.; Schiller, J.; Mel, B. W. An augmented two-layer model captures nonlinear analog spatial integration effects in pyramidal neuron dendrites. *Proceedings of the IEEE* **102** (2014), no. 5, 782–798. doi:10.1109/JPROC.2014.2312671

[33] Katz, Y.; Menon, V.; Nicholson, D. A.; Geinisman, Y.; Kath, W. L.; Spruston, N. Synapse distribution suggests a two-stage model of dendritic integration in CA1 pyramidal neurons. *Neuron* **63** (2009), no. 2, 171–177. doi:10.1016/j.neuron.2009.06.023

[34] Koch, C. *Biophysics of computation: information processing in single neurons*. Oxford University Press, New York–Oxford 2004.

[35] Koch, C.; Poggio, T.; Torre, V. Retinal ganglion cells: a functional interpretation of dendritic morphology. *Phil. Trans. R. Soc. Lond. B* **298** (1982), no. 1090, 227–263. doi:10.1098/rstb.1982.0084

[36] Koch, C.; Poggio, T.; Torre, V. Nonlinear interactions in a dendritic tree: localization, timing, and role in information processing. *Proc. Natl. Acad. Sci. USA* **80** (1983), no. 9, 2799–2802. doi:10.1073/pnas.80.9.2799

[37] Lapicque, L. Recherches quantitatives sur l'excitation électrique des nerfs traitée comme une polarisation. *J. Physiol. Pathol. Gen* **9** (1907), no. 1, 620–635.

[38] Li, S.; Liu, N.; Yao, L.; Zhang, X.; Zhou, D.; Cai, D. Determination of effective synaptic conductances using somatic voltage clamp. *PLoS Computational Biology* **15** (2019), no. 3, e1006871. doi:10.1371/journal.pcbi.1006871

[39] Li, S.; Liu, N.; Zhang, X.; McLaughlin, D. W.; Zhou, D.; Cai, D. Dendritic computations captured by an effective point neuron model. *Proc. Natl. Acad. Sci. USA* **116** (2019), no. 30, 15244–15252. doi:10.1073/pnas.1904463116

[40] Li, S.; Liu, N.; Zhang, X.-h.; Zhou, D.; Cai, D. Bilinearity in spatiotemporal integration of synaptic inputs. *PLoS Computational Biology* **10** (2014), no. 12, e1004014. doi:10.1371/journal.pcbi.1004014

[41] Li, S.; Zhou, D.; Cai, D. Analysis of the dendritic integration of excitatory and inhibitory inputs using cable models. *Commun. Math. Sci.* **13** (2015), no. 2, 565–575. doi:10.4310/CMS.2015.v13.n2.a16

[42] London, M.; Häusser, M. Dendritic computation. *Annu. Rev. Neurosci.* **28** (2005), 503–532. doi:10.1146/annurev.neuro.28.061604.135703

[43] Longordo, F.; To, M.-S.; Ikeda, K.; Stuart, G. J. Sublinear integration underlies binocular processing in primary visual cortex. *Nature Neuroscience* **16** (2013), no. 6, 714–723. doi:10.1038/nn.3394

[44] Magee, J. C. Dendritic hyperpolarization-activated currents modify the integrative properties of hippocampal CA1 pyramidal neurons. *The Journal of Neuroscience* **18** (1998), no. 19, 7613–7624. doi:10.1523/JNEUROSCI.18-19-07613.1998

[45] Magee, J. C. Dendritic integration of excitatory synaptic input. *Nature Reviews Neuroscience* **1** (2000), no. 3, 181–190. doi:10.1038/35044552

[46] Magee, J. C.; Cook, E. P. Somatic EPSP amplitude is independent of synapse location in hippocampal pyramidal neurons. *Nature Neuroscience* **3** (2000), no. 9, 895–903. doi:10.1038/78800

[47] Magee, J. C.; Johnston, D. Characterization of single voltage-gated Na+ and Ca2+ channels in apical dendrites of rat CA1 pyramidal neurons. *The Journal of Physiology* **487** (1995), 67–90. doi:10.1113/jphysiol.1995.sp020862

[48] Major, G.; Evans, J. D.; Jack, J. Solutions for transients in arbitrarily branching cables: I. Voltage recording with a somatic shunt. *Biophysical Journal* **65** (1993), no. 1, 423–449. doi:10.1016/S0006-3495(93)81037-3

[49] Major, G.; Larkman, A. U.; Jonas, P.; Sakmann, B.; Jack, J. J. Detailed passive cable models of whole-cell recorded CA3 pyramidal neurons in rat hippocampal slices. *Journal of Neuroscience* **14** (1994), no. 8, 4613–4638. doi:10.1523/JNEUROSCI.14-08-04613.1994

[50] Migliore, M.; Hoffman, D.; Magee, J.; Johnston, D. Role of an A-type K+ conductance in the back-propagation of action potentials in the dendrites of hippocampal pyramidal neurons. *Journal of Computational Neuroscience* **7** (1999), no. 1, 5–15. doi:10.1023/A:1008906225285

[51] Morris, C.; Lecar, H. Voltage oscillations in the barnacle giant muscle fiber. *Biophysical Journal* **35** (1981), no. 1, 193–213. doi:10.1016/S0006-3495(81)84782-0

[52] Nicholson, D. A.; Trana, R.; Katz, Y.; Kath, W. L.; Spruston, N.; Geinisman, Y. Distance-dependent differences in synapse number and AMPA receptor expression in hippocampal CA1 pyramidal neurons. *Neuron* **50** (2006), no. 3, 431–442. doi:10.1016/j.neuron.2006.03.022

[53] Poirazi, P.; Brannon, T.; Mel, B. W. Arithmetic of subthreshold synaptic summation in a model CA1 pyramidal cell. *Neuron* **37** (2003), no. 6, 977–987. doi:10.1016/S0896-6273(03)00148-X

[54] Poirazi, P.; Brannon, T.; Mel, B. W. Pyramidal neuron as two-layer neural network. *Neuron* **37** (2003), no. 6, 989–999. doi:10.1016/S0896-6273(03)00149-1

[55] Poleg-Polsky, A.; Mel, W. B.; Schiller, J. Neuronal shape parameters and substructures as a basis of neuronal form. *Nature Neuroscience* (2004), 621–627.

[56] Rall, W. Theory of physiological properties of dendrites. *Annals of the New York Academy of Sciences* **96** (1962), no. 4, 1071–1092. doi:10.1111/j.1749-6632.1962.tb54120.x

[57] Rall, W. Theoretical significance of dendritic trees for neuronal input-output relations. *Neural Theory and Modeling* (1964), 73–97.

[58] Rall, W. Distinguishing theoretical synaptic potentials computed for different soma-dendritic distributions of synaptic input. *Journal of Neurophysiology* **30** (1967), no. 5, 1138–1168. doi:10.1152/jn.1967.30.5.1138

[59] Rall, W.; Burke, R.; Holmes, W.; Jack, J.; Redman, S.; Segev, I. Matching dendritic neuron models to experimental data. *Physiological Reviews* **72** (1992), suppl. 4, S159–S186. doi:10.1152/physrev.1992.72.suppl_4.S159

[60] Rall, W.; Burke, R.; Smith, T.; Nelson, P.; Frank, K. Dendritic location of synapses and possible mechanisms for the monosynaptic EPSP in motoneurons. *Journal of neurophysiology* **30** (1967), 1169–1193. doi:10.1152/jn.1967.30.5.1169

[61] Rall, W.; Rinzel, J. Branch input resistance and steady attenuation for input to one branch of a dendritic neuron model. *Biophysical Journal* **13** (1973), no. 7, 648–688. doi:10.1016/S0006-3495(73)86014-X

[62] Rall, W.; Shepherd, G. M.; Reese, T. S.; Brightman, M. W. Dendrodendritic synaptic pathway for inhibition in the olfactory bulb. *Experimental Neurology* **14** (1966), no. 1, 44–56. doi:10.1016/0014-4886(66)90023-9

[63] Rapp, M.; Segev, I.; Yarom, Y. Physiology, morphology and detailed passive models of guinea-pig cerebellar Purkinje cells. *The Journal of Physiology* **474** (1994), no. 1, 101–118. doi:10.1113/jphysiol.1994.sp020006

[64] Redman, S.; Walmsley, B. The time course of synaptic potentials evoked in cat spinal motoneurones at identified group Ia synapses. *The Journal of Physiology* **343** (1983), no. 1, 117–133. doi:10.1113/jphysiol.1983.sp014884

[65] Ringach, D.; Shapley, R. Reverse correlation in neurophysiology. *Cognitive Science* **28** (2004), no. 2, 147–166. doi:10.1207/s15516709cog2802_2

[66] Rinzel, J.; Rall, W. Transient response in a dendritic neuron model for current injected at one branch. *Biophysical Journal* **14** (1974), no. 10, 759–790. doi:10.1016/S0006-3495(74)85948-5

[67] Rose, R. M.; Hindmarsh, J. L. The assembly of ionic currents in a thalamic neuron I. The three-dimensional model. *Proceedings of the Royal Society of London. B. Biological Sciences* **237** (1989), no. 1288, 267–288. doi:10.1098/rspb.1989.0049

[68] Schiller, J.; Schiller, Y.; Stuart, G.; Sakmann, B. Calcium action potentials restricted to distal apical dendrites of rat neocortical pyramidal neurons. *The Journal of Physiology* **505** (1997), no. 3, 605–616. doi:10.1111/j.1469-7793.1997.605ba.x

[69] Schmidt-Hieber, C.; Toleikyte, G.; Aitchison, L.; Roth, A.; Clark, B. A.; Branco, T.; Häusser, M. Active dendritic integration as a mechanism for robust and precise grid cell firing. *Nature Neuroscience* **20** (2017), no. 8, 1114–1121. doi:10.1038/nn.4582

[70] Segev, I.; London, M. Untangling dendrites with quantitative models. *Science* **290** (2000), no. 5492, 744–750. doi:10.1126/science.290.5492.744

[71] Segev, I.; Rinzel, J.; Shepherd, G. M. *The theoretical foundation of dendritic function: the collected papers of Wilfrid Rall with commentaries*. MIT Press, Cambridge, Mass., 2003.

[72] Smith, G. D.; Cox, C. L.; Sherman, S. M.; Rinzel, J. Fourier analysis of sinusoidally driven thalamocortical relay neurons and a minimal integrate-and-fire-or-burst model. *Journal of Neurophysiology* **83** (2000), no. 1, 588–610. doi:10.1152/jn.2000.83.1.588

[73] Smith, M. A.; Ellis-Davies, G. C.; Magee, J. C. Mechanism of the distance-dependent scaling of Schaffer collateral synapses in rat CA1 pyramidal neurons. *The Journal of Physiology* **548** (2003), no. 1, 245–258. doi:10.1111/j.1469-7793.2003.00245.x

[74] Spruston, N. Pyramidal neurons: dendritic structure and synaptic integration. *Nature Reviews Neuroscience* **9** (2008), no. 3, 206–221. doi:10.1038/nrn2286

[75] Spruston, N.; Jaffe, D. B.; Johnston, D. Dendritic attenuation of synaptic potentials and currents: the role of passive membrane properties. *Trends in Neurosciences* **17** (1994), no. 4, 161–166. doi:10.1016/0166-2236(94)90094-9

[76] Spruston, N.; Stuart, G.; Häusser, M. Principles of dendritic integration. *Dendrites*, 351–398. Oxford University Press, Oxford, 2016. doi:10.1093/acprof:oso/9780198745273.001.0001

[77] Steriade, M. Cortical long-axoned cells and putative interneurons during the sleep-waking cycle. *Behavioral and Brain Sciences* **1** (1978), no. 3, 465–485. doi:10.1017/S0140525X00076111

[78] Steriade, M.; Deschênes, M.; Oakson, G. Inhibitory processes and interneuronal apparatus in motor cortex during sleep and waking. I. Background firing and responsiveness of pyramidal tract neurons and interneurons. *Journal of Neurophysiology* **37** (1974), no. 5, 1065–1092.

[79] Stuart, G.; Spruston, N. Determinants of voltage attenuation in neocortical pyramidal neuron dendrites. *The Journal of Neuroscience* **18** (1998), no. 10, 3501–3510. doi:10.1523/JNEUROSCI.18-10-03501.1998

[80] Stuart, G. J.; Spruston, N. Dendritic integration: 60 years of progress. *Nature Neuroscience* **18** (2015), no. 12, 1713–1721. doi:10.1038/nn.4157

[81] Timofeeva, Y.; Cox, S. J.; Coombes, S.; Josić, K. Democratization in a passive dendritic tree: an analytical investigation. *Journal of Computational Neuroscience* **25** (2008), no. 2, 228–244. doi:10.1007/s10827-008-0075-9

[82] Tuckwell, H. C. *Introduction to theoretical neurobiology. Volume 1: Linear cable theory and dendritic structure*. Cambridge University Press, Cambridge, 1988. doi:10.1017/CBO9780511623271

[83] Ujfalussy, B. B.; Makara, J. K.; Lengyel, M.; Branco, T. Global and multiplexed dendritic computations under in vivo-like conditions. *Neuron* **100** (2018), no. 3, 579–592. doi:10.1016/j.neuron.2018.08.032

[84] Vida, I.; Bartos, M.; Jonas, P. Shunting inhibition improves robustness of gamma oscillations in hippocampal interneuron networks by homogenizing firing rates. *Neuron* **49** (2006), no. 1, 107–117. doi:10.1016/j.neuron.2005.11.036

[85] Xu, N.-l.; Harnett, M. T.; Williams, S. R.; Huber, D.; O'Connor, D. H.; Svoboda, K.; Magee, J. C. Nonlinear dendritic integration of sensory and motor input during an active sensing task. *Nature* **492** (2012), no. 7428, 247–251. doi:10.1038/nature11601

[86] Zador, A.; Agmon-Snir, H.; Segev, I. The morphoelectrotonic transform: a graphical approach to dendritic function. *The Journal of Neuroscience* **15** (1995), no. 3, 1669–1682. doi:10.1523/JNEUROSCI.15-03-01669.1995

[87] Zhao, X.; Liu, M.; Cang, J. Sublinear binocular integration preserves orientation selectivity in mouse visual cortex. *Nature Communications* **4** (2013), 2088. doi:10.1038/ncomms3088

[88] Zhou, D.; Li, S.; Zhang, X.-h.; Cai, D. Phenomenological incorporation of nonlinear dendritic integration using integrate-and-fire neuronal frameworks. *PloS One* **8** (2013), no. 1, e53508. doi:10.1371/journal.pone.0053508

SONGTING LI
Institute of Natural Sciences
Shanghai Jiao Tong University
800 Dongchuan Rd.
Shanghai, 200240
CHINA
E-mail: songting@sjtu.edu.cn

DOUGLAS ZHOU
Institute of Natural Sciences
Shanghai Jiao Tong University
800 Dongchuan Rd.
Shanghai, 200240
CHINA
E-mail: zdz@sjtu.edu.cn

DAVID W. MCLAUGHLIN
Courant Institute
251 Mercer St.
New York, NY 10012
USA
E-mail: david.mclaughlin@nyu.edu

Received May 2020.
Revised November 2020.